Resource

Cell Chemical Biology

A Robust, GFP-Orthogonal Photoswitchable Inhibitor Scaffold Extends Optical Control over the Microtubule Cytoskeleton

Graphical Abstract

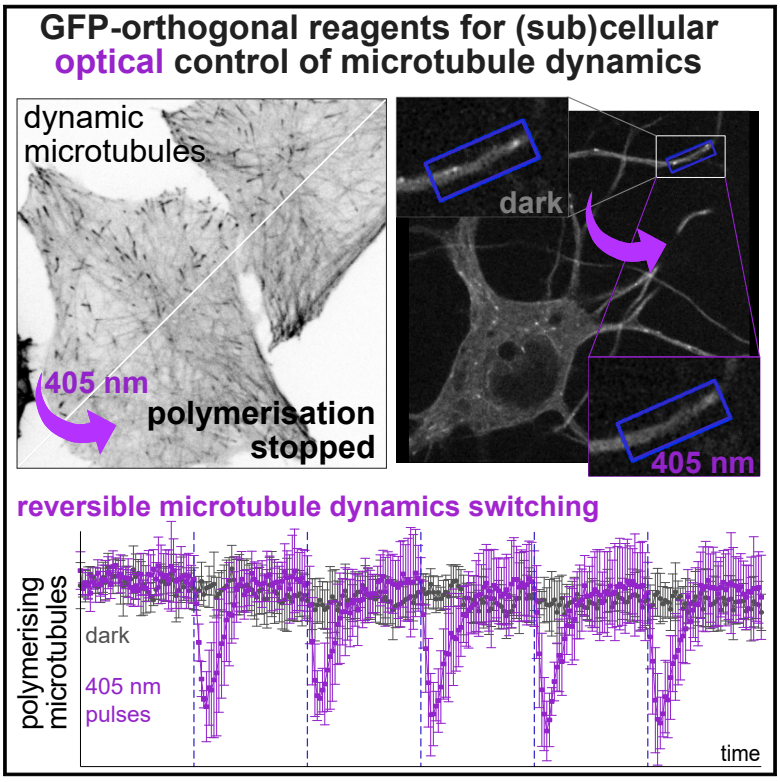

Authors

Li Gao, Joyce C.M. Meiring, ..., Julia Ahlfeld, Anna Akhmanova, Michel O. Steinmetz, Oliver Thorn-Seshold

Correspondence

oliver.thorn-seshold@cup.lmu.de

In Brief

Photocontrollable reagents have unique potential as high spatiotemporal precision modulators of biological systems. Here, Gao et al. demonstrate a GFP-orthogonal and metabolically stable photoswitch that allows optical control over microtubule dynamics and architecture with subcellular resolution. The photoswitch scaffold also offers new possibilities for photopharmaceutical design against other targets.

Highlights

- SBTub3 photocontrols microtubule dynamics, organization, and dependent processes
- Microtubule photocontrol is cell and sub-cellularly precise and temporally reversible
- SBT photocontrol is orthogonal to GFP/YFP imaging and SBTs are metabolically stable
- The SBT scaffold is promising for photopharmaceuticals for other protein targets

Gao et al., 2021, Cell Chemical Biology *28*, 228–241
February 18, 2021
https://doi.org/10.1016/j.chembiol.2020.11.007

CellPress

CellPress

Cell Chemical Biology

Resource

A Robust, GFP-Orthogonal Photoswitchable Inhibitor Scaffold Extends Optical Control over the Microtubule Cytoskeleton

Li Gao,[1] Joyce C.M. Meiring,[2] Yvonne Kraus,[1] Maximilian Wranik,[3] Tobias Weinert,[3] Stefanie D. Pritzl,[4] Rebekkah Bingham,[1] Evangelia Ntouliou,[1] Klara I. Jansen,[2] Natacha Olieric,[3] Jörg Standfuss,[3] Lukas C. Kapitein,[2] Theobald Lohmüller,[4] Julia Ahlfeld,[1] Anna Akhmanova,[2] Michel O. Steinmetz,[3,5] and Oliver Thorn-Seshold[1,6,*]

[1]Department of Pharmacy, Ludwig-Maximilians University of Munich, Munich 81377, Germany

[2]Cell Biology, Neurobiology and Biophysics, Department of Biology, Faculty of Science, Utrecht University, Utrecht 3584, Netherlands

[3]Laboratory of Biomolecular Research, Division of Biology and Chemistry, Paul Scherrer Institut, Villigen 5232, Switzerland

[4]Chair for Photonics and Optoelectronics, Nano-Institute Munich, Department of Physics, Ludwig-Maximilians University of Munich, Munich 80539, Germany

[5]Biozentrum, University of Basel, Basel 4056, Switzerland

[6]Lead Contact

*Correspondence: oliver.thorn-seshold@cup.lmu.de

https://doi.org/10.1016/j.chembiol.2020.11.007

SUMMARY

Optically controlled chemical reagents, termed "photopharmaceuticals," are powerful tools for precise spatiotemporal control of proteins particularly when genetic methods, such as knockouts or optogenetics are not viable options. However, current photopharmaceutical scaffolds, such as azobenzenes are intolerant of GFP/YFP imaging and are metabolically labile, posing severe limitations for biological use. We rationally designed a photoswitchable "SBT" scaffold to overcome these problems, then derivatized it to create exceptionally metabolically robust and fully GFP/YFP-orthogonal "SBTub" photopharmaceutical tubulin inhibitors. Lead compound SBTub3 allows temporally reversible, cell-precise, and even subcellularly precise photomodulation of microtubule dynamics, organization, and microtubule-dependent processes. By overcoming the previous limitations of microtubule photopharmaceuticals, SBTubs offer powerful applications in cell biology, and their robustness and druglikeness are favorable for intracellular biological control in *in vivo* applications. We furthermore expect that the robustness and imaging orthogonality of the SBT scaffold will inspire other derivatizations directed at extending the photocontrol of a range of other biological targets.

INTRODUCTION

The microtubule (MT) cytoskeleton supports an extraordinary range of cellular functions simultaneously, with central roles in nearly all directional processes, such as intracellular transport and cell motility; its crucial function in cell proliferation has also made it a prominent anticancer drug target (Dumontet and Jordan, 2010; Peterson and Mitchison, 2002). Although cytoskeleton research typically aims to study a subset of MT-dependent processes that are spatially and/or temporally localized, nearly all small-molecule inhibitors of MTs (drugs such as paclitaxel, colchicine, epothilone, etc.) cannot be spatiotemporally directed, so they inhibit MT dynamics throughout cells and systems to which they are applied (Janke and Steinmetz, 2015). For decades this restricted the scope of inhibition studies of MT biology.

Recently, the advent of optically targeted tools to manipulate biological systems with increased spatiotemporal precision has revolutionized diverse fields of biological research, particularly for temporally regulated and geometrically complex systems. Optogenetics, photouncaging approaches, and photoswitchable small-molecule inhibitors or "photopharmaceuticals," have all been developed as optically targeted tools, with distinct strengths and weaknesses (Wittmann et al., 2020). Photopharmaceuticals offer performance and applications that are quite distinct from the other methods. Unlike photouncaging, they feature near-instantaneous photoresponse without byproduct generation, and can offer reversible switching (Klán et al., 2013). As distinct from optogenetics, they possess the advantages of small-molecule inhibitors: they do not require genetic engineering; they can directly address critical proteins (such as tubulin), which due to their structure may not permit functional control through fusion to optogenetically active domains; they also offer easy transition between model systems as well as potential for therapeutic applications (Hüll et al., 2018; Zenker et al., 2017). Motivated by the spatiotemporal complexity and critical importance of MT cytoskeleton biology, the search for photopharmaceutical MT-modulating reagents has intensified in recent years (Castle and Odde, 2015).

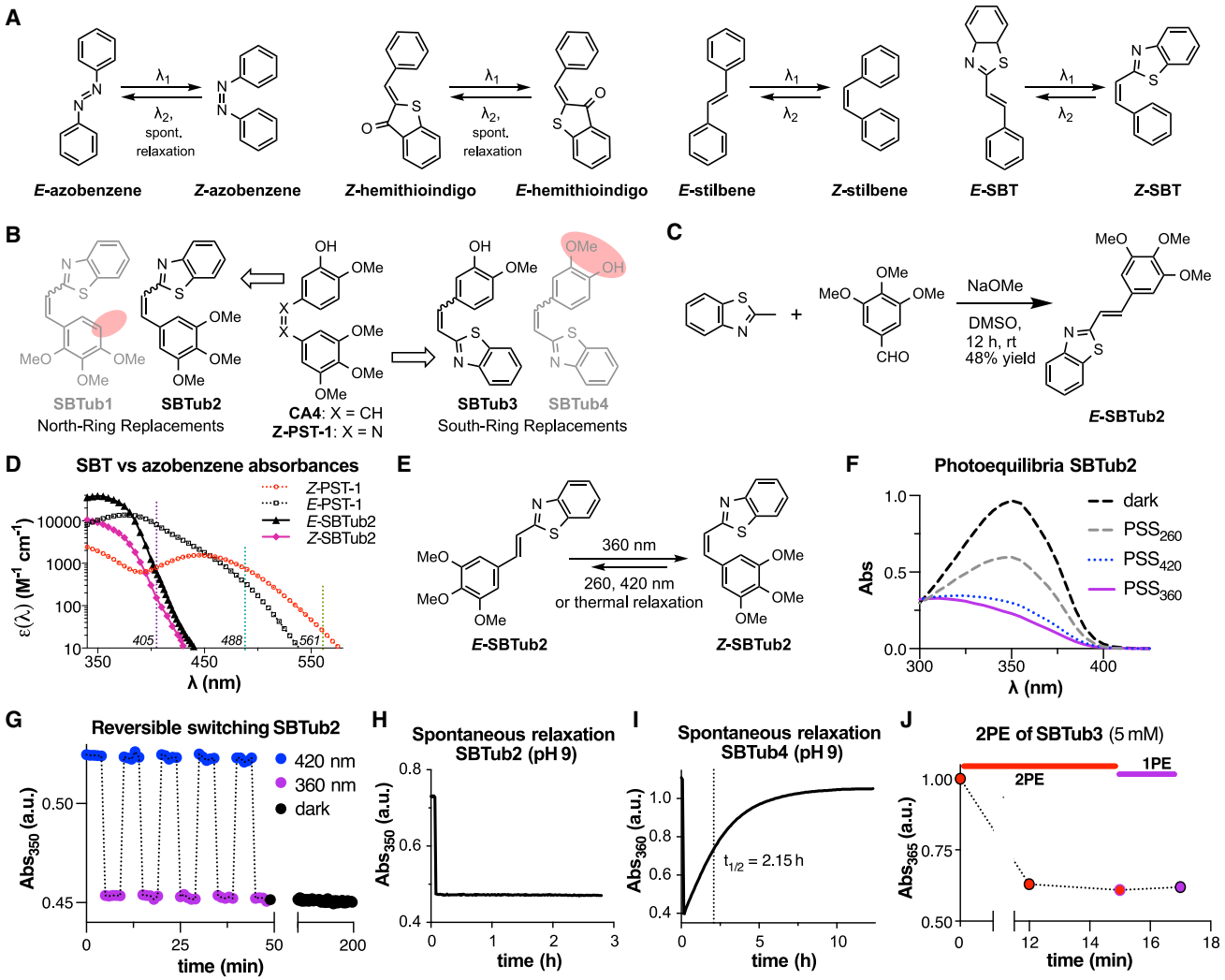

Figure 1. Design, Synthesis and Photoswitching of SBTubs

(A) Photoswitchable molecular scaffolds azobenzene, hemithioindigo, stilbene, and styrylbenzothiazole (SBT).

(B) SBTubs designed by derivatizing SBTs so that their *Z* isomers mimic (SBTub2/3) or mismatch (SBTub1/4) the tubulin-binding pharmacophore of combretastatin A-4 (CA4) and of azobenzene photopharmaceutical PST-1. Mismatches indicated by red shaded ovals.

(C) Synthesis of representative reagent, SBTub2.

(D) Comparison of absorbance spectra of representative SBT and azobenzene scaffolds illustrates the SBT's absorption cutoff above 410 nm, which suits it to orthogonality to GFP, YFP, and RFP imaging.

(E) SBTubs can be photoswitched from all-*E* to majority-*Z* using 360 nm, partially switched back with 420 or 260 nm light, and revert quantitatively to all-*E* by thermally driven spontaneous relaxation.

(F) Absorbance spectra of representative SBTub2 at various photostationary state (PSSs) equilibria.

(G) SBTubs can be photoswitched in aqueous medium under air over multiple cycles without degradation (see also Figures S1B–S1J). At pH ~7 they persist at PSS without appreciable spontaneous relaxation for hours when illumination is stopped.

(H and I) Spontaneous relaxation of (H) SBTub2 and (I) SBTub4 at pH ~9 shows the structure-dependent influence of solvent environment on relaxation rates (see also Figure S1C).

(J) SBTubs can be isomerized via two-photon excitation (2PE) reaching identical PSS as under single-photon excitation (1PE) (2PE at 780 nm, 1PE at 360 nm; compare Figure S1D).

The vast majority of photopharmaceuticals continue to be based on the reversibly photoswitchable azobenzene molecular scaffold, in which an abiotic N=N chromophore underlies photoswitching between the stable *E* and metastable *Z* isomers (Figure 1A) (Broichhagen et al., 2015). The most widely used photopharmaceuticals for optical MT control are also azobenzene based. These "photostatins" (PSTs) (Figure 1B) are analogs of the tubulin depolymerizing agent combretastatin A-4 (CA4) (Figure 1B) (Borowiak et al., 2015; Engdahl et al., 2015; Gaspari et al., 2017; Sheldon et al., 2016). Driven by illuminations with low-intensity visible light, PSTs undergo bidirectional photoswitching between the inactive *E* and the MT-inhibiting *Z* isomer. PST photoswitching has enabled noninvasive, reversible, cellularly resolved optical control over MT dynamics and network

structure in cell culture as well as *Drosophila melanogaster* (Singh et al., 2018), *Caenorhabditis elegans* (Borowiak et al., 2015), *Danio rerio* (Vandestadt et al., 2019), and mouse models (Zenker et al., 2017), helping to resolve questions in mammalian development and neuroscience (Eguchi et al., 2017; Zenker et al., 2018). These illustrate the power of photopharmacology to enable previously inaccessible studies of spatiotemporally complex processes. However, azobenzene-based approaches to photocontrol of intracellular biology in general incur three disadvantages.

Firstly, intracellular photopharmacology typically relies on imaging-based readouts, but azobenzenes usually feature such a strong uni- or bidirectional photoresponse to standard imaging wavelengths, that isomerization caused by imaging overrides their desired photoswitching (Borowiak et al., 2015; Hüll et al., 2018) and/or limits the scope of experiments. This photoresponse is due to the low-energy $n \rightarrow \pi^*$ transitions of their N=N chromophore's lone pairs. Regardless of their starting isomer population, azobenzenes, such as PSTs, are rapidly switched to ~3:1 *E*:*Z* under 488 nm (GFP/fluorescein imaging) and to ~4:1 *E*:*Z* under 514 nm (YFP/Cy3); even 561 nm illumination noticeably affects isomer ratios on the confocal stage. Therefore, due to imaging, a background of *Z*-azobenzene is created in areas where isomerization away from the stable *E* isomer is not desired; and in areas where most *Z* isomer is generated (typically by photoswitching at 405 nm), each imaging frame instead increases the proportion of *E* isomer. By counteracting any spatiotemporally resolved isomer patterning throughout the sample, non-orthogonality to imaging wavelengths limits the azobenzene scaffold's potential for high-precision use in cell biology or transgenic animals (where the most common tags are GFP/YFP-based).

Secondly, azobenzene photopharmaceuticals for intracellular targets tend to lose performance when transitioning to cellular assays, which seems to be due to the cellular instability of their electrophilic and abiotic N=N chromophore (Schehr et al., 2019). The majority of azobenzenes can be degraded following the addition of cytoplasmic glutathione (GSH) (ca. 3–10 mM) to the N=N group, ultimately giving a range of non-photoswitchable byproducts of N=N bond degradation (Lei et al., 2019; Samanta et al., 2013a, 2013b; Sheldon et al., 2016). Cleavage byproducts may in many cases be *more* bioactive on target than the intact reagent, which blocks cellular photoswitchability of inhibition (Schehr et al., 2019). This is a major flaw of the prevailing design strategy of "azo-extension," which ensures that only half of the photoswitch is properly accommodated by the protein target, despite the known risks of scission. Even when cellularly photoswitchable reagents are designed by pharmacophore embedding, such that scission byproducts cannot be bioactive on target (such as PSTs), they typically feature losses of apparent potency that are presumably due to such degradation. For example, PSTs are ~2 orders of magnitude less potent in cells than CA4, despite near-identical potency in cell-free assays. Potency loss and potentially problematic metabolites continue to obstruct robust applications of azobenzenes to intracellular targets, especially *in vivo* (Boulègue et al., 2007; Sheldon et al., 2016).

Thirdly, azobenzenes undergo spontaneous unidirectional $Z \rightarrow E$ isomer relaxation, the rate of which depends on the substituents at the six *ortho* and *para* positions that interact strongly with the N=N double bond. In particular, some of the most important functional groups for ligand-protein interactions (including hydroxy, amine, and thiol groups) cause fast relaxation in physiological aqueous medium if they substitute at any of these positions, typically giving μs–ms half-lives (Hüll et al., 2018; Samanta et al., 2013b). Fast-relaxing azobenzenes cannot practicably be photopatterned to address intracellular targets, since counteracting their uniform relaxation to the *E* isomer would require biologically unacceptable photon fluxes. Azobenzene photopharmacology is in general limited by the ranges of relaxation half-lives accessible to its tolerated substituent space, which also probably restricts its target scope.

These problems—non-orthogonality to standard imaging conditions, metabolic liabilities in intracellular settings, and strong substituent-dependent limits on thermal half-life—intrinsically derive from azobenzene's N=N double bond. We perceive that these problems have largely hindered the translation of azobenzene photopharmaceuticals for intracellular targets from cell-free to cell culture settings, and essentially block their applications from simple *in vivo* models to higher animals (for further discussion, see the Supplemental Information). Therefore, we were motivated to develop new photoswitchable scaffolds avoiding these three problems—both for the specific case of photoswitchable MT inhibitors, as well as for general applications to chemical biology—and to examine their performance features that could suit them to more robust, orthogonal, biological photocontrol in complex systems.

In light of these three problems, we here explored the almost-unstudied styrylbenzothiazole (SBT) molecular scaffold as an alternative photoswitch based on a C=C double bond that could avoid these three problems. We evaluated this scaffold for chemical biology by synthesizing a rationally designed series of SBT-based tubulin inhibitors (SBTubs) and assaying them for their performance as biochemically robust, GFP-orthogonal, photoswitchable analogs of CA4. We obtained ligand-protein crystal structures confirming the SBTubs' two modes of tubulin binding, then demonstrated their optical control over MT network integrity, cell division, and cell death. Finally, using their unique photoresponse characteristics, we demonstrate that they enable temporally reversible, optical modulation of MT dynamics independently of ongoing imaging, in live GFP-tagged cells, and demonstrate their capacity for subcellularly spatially resolved and temporally precise inhibition of endogenous MT dynamics in primary hippocampal neurons. This is to our knowledge the first use of SBTs as photopharmaceuticals in chemical biology, and highlights both SBTubs' and the SBT scaffold's promise for use in a range of high spatiotemporal precision biological studies.

RESULTS

Scaffold Selection

To avoid photoresponse to wavelengths above 460 nm, we chose a photoswitch based on a C=C double bond that has no chromophore lone pairs and so no n-π^* bands (Horspool and Lenci, 2004), yet offers substantial geometric change upon isomerization so that bioactivity photoswitching could be possible. Hemithioindigo is the most widely used C=C-based photoswitch, but we excluded it because of its long-wavelength response even at 520 nm, due to the *ipso*-sulfur (Sailer et al.,

2020). Stilbenes are barely used in modern photopharmacology since they require UV light below 340 nm for photoswitching, which is not accessible on microscopes, and also degrade when illuminated in the presence of oxygen (Francioso et al., 2014). We instead selected the almost-unstudied SBT scaffold. SBT is a C=C double bond-based photoswitch whose planar *E* and bent *Z* isomers differ substantially in geometric fit and end-to-end distance. They have similar geometry as the azobenzene *E* and *Z* isomers, although they are larger on their benzothiazole side (Figure 1A). We expected that the non-electrophilic C=C double bond (Awad et al., 2013; Hofmann, 1880) would endow them with increased robustness toward GSH reduction as well as slower relaxation of the *Z* isomer, as compared with azobenzenes; while, as compared with stilbenes, the benzothiazole would redshift the π-π^* band enough to be photoswitched with visible light (Mishra et al., 2013) while also blocking photochemical degradation (El-Hendawy et al., 2015).

Reagent Design and Synthesis

Searching for isomer-dependently bioactive tubulin inhibitors based on the SBT scaffold, we designed two SBTubs whose *Z* isomers could be closely isosteric replacements of the MT inhibitor CA4 and whose *E isomer*s would mimic the inactive *trans*-CA4, so aiming at *Z*-SBTub-specific MT inhibition. These became SBTub2 (where the benzothiazole ring replaces the "north," isovanillinyl ring of CA4), and SBTub3 (where the benzothiazole replaces the "south," trimethoxyphenyl ring; Figure 1B). We expected that the benzothiazole would give similar space occupancy, geometry, and polarity intermediate as the replaced rings, and since the colchicine site is somewhat accommodating (Shan et al., 2011; Tron et al., 2006), we expected that both *Z*-SBTubs might bind despite sacrificing some potency-enhancing interactions.

As a key validation step, we also created permutation controls (designed-inactive compounds) to test the tubulin specificity and *Z* isomer specificity of SBTub bioactivity. Permutation controls contain the same number and types of functional groups, but swap the positions of key bioactivity-controlling substituents to intentionally mismatch requirements for target-specific binding. We have previously used this to distinguish effects of molecularly specific binding to the target protein (which should be a feature of the designed-active compounds only) versus "pan-assay interference compounds"-like nonspecific bioactive effects expected for typically hydrophobic photoswitch compounds (e.g., promiscuous binding to or aggregation on proteins, compound precipitation, membrane disruption [Baell and Nissink, 2018]) as well as nonspecific scaffold toxicity or phototoxicity under illumination, since any nonspecific bioactivity should be reproduced by permutation controls (Sailer et al., 2019). We permuted methoxy and hydro groups of SBTub2 to create control SBTub1, and permuted hydroxy and methoxy groups of SBTub3 to create control SBTub4 (Figure 1B). Reagents SBTub1–4 were synthesized in good yields by basic aldol condensations of 2-methylbenzothiazole with the corresponding aldehydes (Figure 1C; see the Supplemental Information).

SBTub Spectral Response in Cuvette Suggests Orthogonality to GFP Imaging

The spectral characteristics of SBTubs were similar, with $\pi \rightarrow \pi^*$ absorption maxima for *E* ($\sim$360 nm) and *Z* isomers ($\sim$305 nm) being well separated, enabling directional photoisomerizations with LEDs at wavelengths $\leq$425 nm (Figures S1A–S1D). Pleasingly, both *E*- and *Z*-SBT isomers' absorptions drop sharply toward zero above 410 nm (Figure 1D). This is crucial for avoiding any $E \leftrightarrow Z$ photoisomerization under 488 nm imaging with intense focused lasers ("GFP-orthogonality") because absorption "tails" that extend far past absorbance maxima can cause substantial photoswitching in microscopy (e.g., 561 nm RFP imaging on the confocal microscope photoisomerizes the azobenzene *Z*-PST, although its absorbance maximum is at 445 nm). Our expectation was therefore, that the SBTubs' absorption cutoff is at the optimum position to permit rapid $E \rightarrow Z$ photoswitching with the common 405 nm microscopy laser line, while potentially allowing GFP-orthogonality.

SBTub Photoswitching Is Robust across a Range of pH and Environments

Under physiological conditions, the SBTubs could be optimally $E \rightarrow Z$ photoisomerized with 360 nm light, giving a photostationary state (PSS) equilibrium with a *Z*:*E* ratio of $\sim$85:15. Applying shorter or longer wavelengths back-isomerized the SBTubs toward more *E*-enriched PSSs (Figures 1E and 1F). We selected "dark" (all-*E*) and "lit" (360 nm, mostly-*Z*) as default illumination conditions for further use (Berdnikova et al., 2012). Pleasingly for our aims, reversible photoisomerizations with high-power illuminations repeatedly traversing the biologically applicable range of 360–420 nm caused no detectable photodegradation under aerobic aqueous conditions (Figure 1G). The SBTub spectra and photoswitching properties were entirely robust to variations of pH and environment (Figures S1C and S1D). The functional performance of this first generation of slow-relaxing SBTubs is turn-on-only, due to the band overlap between *E* and *Z* isomers. However, the metastable *Z* isomers of all SBTubs could be quantitatively relaxed to *E* by warming to 50°C–60°C overnight, although at 25°C they showed no significant thermal relaxation after several hours at pH $\sim$7 in physiological medium (Figure 1G). The *para*-hydroxy group unique to SBTub4 accelerated its relaxation in basic conditions (Figures 1H and 1I), but the stability of *Z*-SBTub4 against relaxation at pH $\sim$7 contrasts favorably to both azobenzene and hemithioindigo photoswitches with *para*- (or *ortho*-) hydroxy or amino substituents that typically feature millisecond (azobenzene) to second (hemithioindigo) half-lives at these conditions. This underlines the broader chemocompatibility of SBTs as a photoswitch scaffold for these functional groups that are so important in ligand design (further discussion in the Supplemental Information).

SBTubs Can Undergo Two-Photon Photoswitching

We tested if SBTubs can be isomerized by two-photon excitation (2PE), which could increase spatial resolution compared with single-photon excitation (1PE) (Moreno et al., 2015). This may especially benefit high spatial precision cell-free studies, such as time-resolved studies of tubulin structural rearrangements following ligand isomerization inside a lattice. We used a mode-locked Ti-sapphire laser at 780 nm to bulk photoisomerize SBTub3 in concentrated (5 mM) DMSO solution, delivering 2PE inside a single voxel and relying on diffusion to establish *Z*/*E*-isomer equilibrium in the whole 8 μL sample. After 12 min of 2PE the isomer equilibrium did not evolve either with additional 2PE or

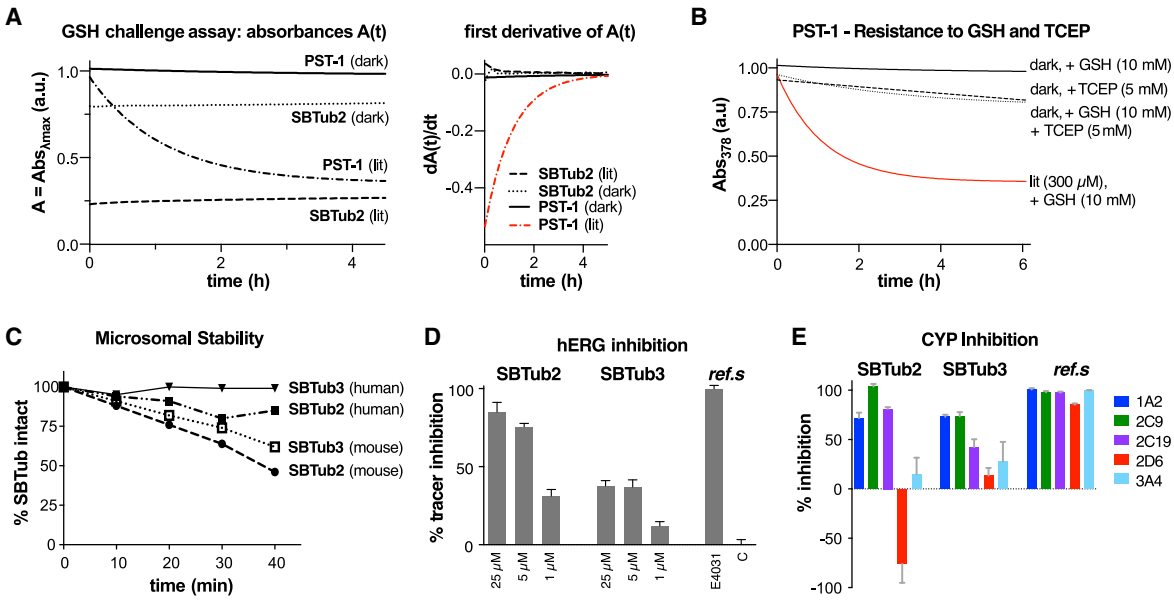

Figure 2. Biochemistry of SBTubs

(A and B) Glutathione (GSH) challenge assays under dark or lit conditions (A) monitoring the change of photoswitch absorbance during incubation with 10 mM GSH of SBT SBTub2 (25 μM) and azobenzene PST-1 (50 μM dark/300 μM lit); decreases indicate molecular degradation. (B) The reducing agent TCEP degrades even the more resistant *E isomer* of PST-1, while *Z*-PST-1 is rapidly degraded by GSH alone (see also Figures S2A–S2F).

(C) SBTub2 and SBTub3 substantially resist metabolism by purified human and mouse liver microsomes (monitored by high-performance liquid chromatography).

(D) hERG binding by SBTub2 and SBTub3, referenced to positive control E4031 (30 μM) and cosolvent-only negative control "C." Data represented as mean with SE, n = 4.

(E) *E*-SBTubs (10 μM) show moderate CYP450 inhibition.

See also Figure S2G.

with 1PE at 360 nm, indicating that 2PE can efficiently photoswitch *E*-SBTub to ~85% *Z* (Figure 1J).

SBTubs Are Highly Robust to Glutathione, and Resist Photobleaching and Metabolism

We next assessed the SBT scaffold's photochemical and biochemical robustness. We monitored *E*- and *Z*-SBTubs under UV irradiation in a Rayonet photochemical reactor. We found them to be stable to 1 h of continuous high-power UV, indicating outstanding photochemical stability (Figures S1E and S1F). We assayed their sensitivity to cellular levels of GSH (10 mM) (Figures 2A and S2A), but detected no degradation, adduct formation, addition-elimination, reduction, or other loss mechanisms. This contrasts strongly to the GSH-mediated destruction of similarly substituted *Z*-azobenzenes, including PST-1 (Figures 2A, 2B, and S2B–S2F; see discussion in the Supplemental Information). We also performed an early *in vitro* metabolic assessment of SBTub2 and SBTub3 for their suitability *in vivo*, examining stability to processing by liver microsomes, inhibition of representative cytochromes, and hERG channel inhibition (Figures 2C–2E). Especially for SBTub3 these assays did not indicate typical drug development problems. As far as we know, only one report has ever considered these crucial biological stability aspects for photoswitches (Babii et al., 2020), and no data are reported for azobenzenes.

We consider the SBT's performance as a photoswitch scaffold, as well as its improved stability and substituent tolerance compared with azobenzenes, promising for further biological applications toward cellular and *in vivo* use. We thus began exploring its applicability as a photopharmaceutical scaffold for cell biology research, through the use of SBTubs as photoswitchable MT inhibitors.

SBTubs Bind to Tubulin and Inhibit Tubulin Polymerization in Their "Lit" State

Since prolonged inhibition of cellular MT dynamics blocks cell proliferation and ultimately results in cell death, we first assayed SBTubs by examining their light-dependent antiproliferative effects on the HeLa cervical cancer cell line (incubation in "lit" conditions via pulsed illuminations with 360 or 420 nm light, or else "dark"). Both SBTub2 and SBTub3 were photoswitchably cytotoxic with ≫20-fold cytotoxicity enhancement when lit at 360 nm (half maximal inhibitory concentration [IC_{50}] ~1–2 μM with ~85% *Z* isomer), as compared with the dark experiments (IC_{50} ≫ 20 μM with ~100% *E* isomer). Crucially, neither permutation control SBTub1/4 displayed significant or light-dependent bioactivity. This supports the suitability of the SBT scaffold for long-term intracellular photopharmacology (Figure 3A). We attribute the weak antiproliferative activity of all SBTubs at high concentrations in the dark, equal to that of permutation controls SBTub1/4 under lit conditions, as aggregation-dependent effects from poor solubility of the compounds at high concentrations (known for similar species [Borowiak et al., 2015; Sailer et al., 2019], and examined further below). The light-dependent

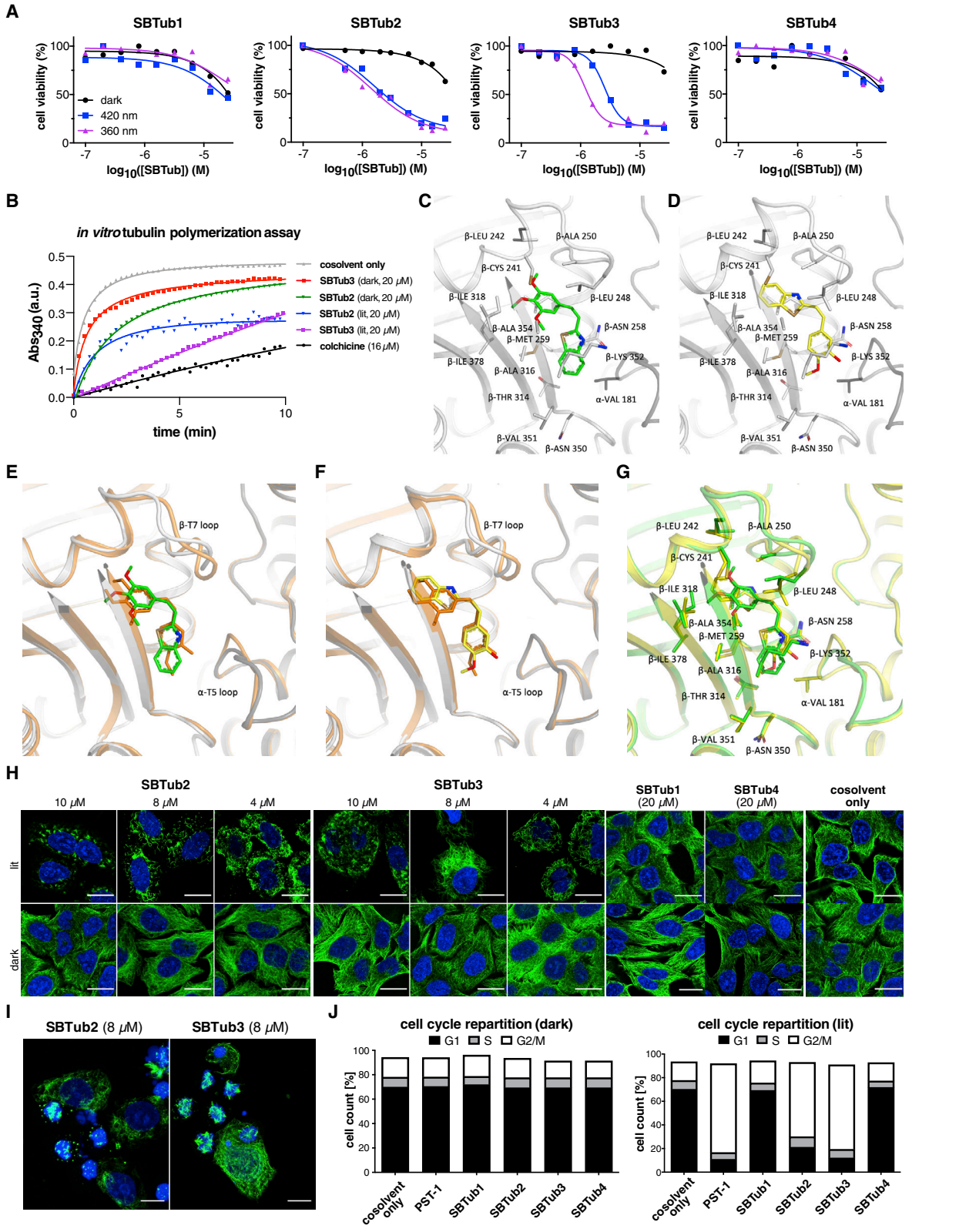

(legend on next page)

activity of the designed-active SBTubs, and the low toxicity of their permutation controls, matched expectations that SBTub2/3's cellular antiproliferative potency should be based primarily on MT inhibition exerted only by the *in-situ*-photogenerated *Z isomer*s binding to the colchicine site.

To examine their molecular mechanism of light-dependent cellular bioactivity, we first assayed the photoswitchably cytotoxic SBTub2/3 for light-dependent inhibition of polymerization of purified tubulin in a cell-free system. *E*-SBTub2/3 were essentially inactive, but their *Z* isomers generated in lit conditions (particularly *Z*-SBTub3) were inhibitors, as expected for colchicine-site ligands (Figure 3B).

Testing the assumption of *Z* isomer-specific tubulin binding at the colchicine site by SBTub2/3, we succeeded in crystallizing *Z*-SBTub2 and *Z*-SBTub3 in complex with the tubulin-DARPin D1 complex (Pecqueur et al., 2012) and solved the structures to 2.05 and 1.86 Å resolution by X-ray crystallography, respectively (Table S1). Both *Z*-SBTub2/3 bind to the colchicine site (at the interface of α- and β-tubulin) (Figures 3C–3G and S3A–S3C). As designed in the ring replacement strategy, they bind with their benzothiazoles in opposite poses, despite contacting identical residues in the binding pocket. *Z*-SBTub2 places its trimethoxyphenyl ring in the "bottom" lobe of the pocket, which is characteristic of trimethoxyphenyl-bearing CA4 analogs (Tron et al., 2006), whereas *Z*-SBTub3 binds with its benzothiazole in the "bottom" lobe to maintain polar interactions at the top lobe with its isovanillyl ring (Figure S3D). The benzothiazole can therefore occupy the same space as either the trimethoxyphenyl or the isovanillyl unit of typical colchicine-site inhibitors (Gaspari et al., 2017). This intriguing top-versus-bottom desymmetrization should assist rational design of SBTub-based photopharmaceuticals that project substituents (e.g., functionally diverse side-chain reporters) outward from the colchicine-binding site.

SBTubs Light Dependently Inhibit MT Function in Cells

We began examining the cellular mechanism of isomer-dependent SBTub bioactivity by imaging the endogenous MT network architecture in cells incubated with *E*/*Z*-SBTubs. Dark assays with *E*-SBTub2/3 had no impact on MT network architecture, but SBTub2/3 lit at 360 nm (mostly-*Z* isomer) caused mitotic arrest and MT depolymerization, with similar dose dependency as in the viability assays (Figure 3H). Z-stack images revealed substantial accumulation of rounded, mitotically arrested cells (Figure 3I). These are hallmarks of treatment with MT-inhibiting antimitotics, supporting the conjecture that SBTub2/3's strongly photoswitchable cytotoxicity arises from their *Z* isomers inhibiting MTs in cells. By contrast, the permutation controls SBTub1/4 showed no disruption of MT network architecture under dark or lit conditions, even at high concentrations which do exert antiproliferative effects (Figure 3H), further supporting that MT-binding activity is specific to photoswitched *Z*-SBTub2/3 only. If their major cellular bioactivity mechanism is MT inhibition, *Z*-SBTub2/3 should induce light-dependent G_2/M phase cell-cycle arrest (Tron et al., 2006), and using flow cytometric analysis we observed this for both *Z*-SBTub2 and 3, but not for their *E* isomers or for permutation controls *E*/*Z*-SBTub1/4 (Figure 3J). This further supports that all-*E*-SBTubs have negligible MT-inhibiting effects, while the appropriately substituted *Z*-SBTub2/3 potently inhibit MT function, suiting them to photoswitching-based control of MT-dependent processes. Observing that, from the two active compounds, SBTub3 was both more reliably soluble than SBTub2, and exhibited a sharper dose-response curve which makes it more suited to isomerization-based bioactivity switching, we selected SBTub3 as our preferred lead compound and performed all subsequent assays with it.

We next set out to test some conceptual advantages that the photophysical and biochemical properties of the SBT scaffold should endow upon the SBTubs, when compared with azobenzenes and other major photoswitch types, in their most likely biological applications.

A Single Isomerization of SBTub Enables Long-Term MT Photocontrol

Since *Z*-SBTubs are stable to cell-free biochemical challenge and to spontaneous relaxation (Figures 1 and 2), we first tested whether a single $E \rightarrow Z$ isomerization event could be used to induce long-term impact on cells, without requiring re-illuminations throughout the assay (as is necessary with faster-relaxing azobenzenes, e.g., PSTs) (Borowiak et al., 2015). We applied *E*-SBTub3 to cell culture, isomerized it *in situ* to a majority-*Z* population using 18 s of low-power LED illumination at 360 nm, then shielded the cells from outside light and observed cell viability

Figure 3. SBTubs' Bioactivity is Light Specific and Tubulin Mediated

(A) SBTub2/3 give strong light-specific antiproliferative effects, while controls SBTub1/4 give minor and light-independent effects (HeLa cells, 40 h incubation; all-*E* dark conditions versus mostly-*Z* lit conditions using low-power pulsed LED illuminations [75 ms per 15 s, <1 mW/cm^2]; one representative experiment of three independent experiments shown).

(B) SBTub2/3 light dependently inhibit tubulin polymerization (turbidimetric *in vitro* polymerization assay; greater absorbance corresponds to a greater degree of polymerization).

(C–G) Close-up views at the colchicine-binding site of X-ray crystal structures of tubulin-*Z*-SBTub complexes (see also Figure S3). (C) Tubulin-*Z*-SBTub2 (PDB: 6ZWC) and (D) tubulin-*Z*-SBTub3 (PDB: 6ZWB) complexes (dark gray α-tubulin and light gray β-tubulin in cartoon representation; ligands and interacting residues in stick representation with oxygens red, nitrogens blue, and ligand carbons green [SBTub2] or yellow [SBTub3]). (E–F) Superimpositions of tubulin-CA4 (orange carbons; PDB: 5LYJ) with (E) tubulin-SBTub2 (green carbons) and (F) tubulin-SBTub3 (yellow carbons) structures. (G) Superimposition of tubulin-SBTub2 (green carbons) and tubulin-SBTub3 (yellow carbons) structures.

(H) Immunofluorescence imaging of cells treated with SBTub2/3 shows breakdown of MT architecture under 360 nm pulsing ("lit") but no disorganization in the dark. Scaffold controls SBTub1/4 and cosolvent controls show no scaffold- or light-dependent confounding effects (HeLa cells, 20 h incubation; α-tubulin in green, DNA stained with DAPI in blue). Scale bars, 20 μm.

(I) Maximum intensity projections along the z axis of SBTub2/3 immunofluorescence image stacks show mitotic arrests in illuminated conditions; treatment as in (H).

(J) Cell-cycle analysis of cells treated with SBTub2/3 shows significant G_2/M arrest under 360 nm pulsing ("lit") but not in the dark, as does reference PST-1. Controls SBTub1/4 and cosolvent show no cell-cycle effects (SBTubs at 20 μM, PST-1 at 2.5 μM).

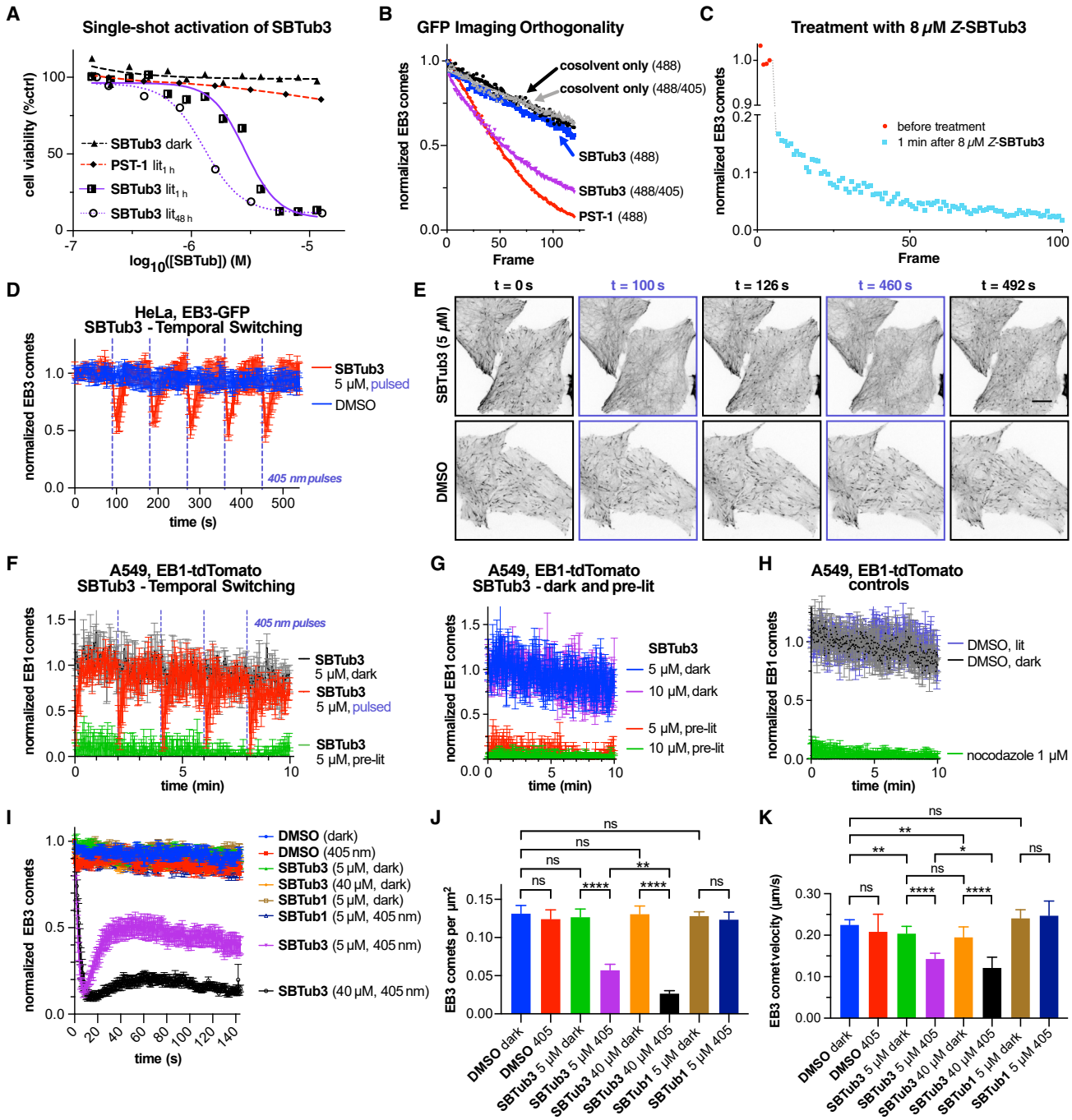

Figure 4. SBTub3 is a GFP-Orthogonal Reagent that When Isomerized Causes Rapidly Reversible Inhibition of MT Dynamics in Live Cells

(A) Antiproliferation assays with single-shot photoactivation ($lit_{1\ h}$) versus with ongoing illumination ($lit_{48\ h}$) show the SBT's sustained pharmacological activity compared with azobenzene PST-1 (HeLa cells, 48 h, pulsing as in Figure 3A; one representative experiment of three independent experiments shown).

(B and C) Live-cell EB3-GFP "comet" counts during GFP imaging with 488 nm (HeLa cells). (B) Imaging in the presence of *E*-SBTub3 does not affect comets, whereas azobenzene PST-1 is isomerized by imaging and stops MT polymerization. Only with additional 405 nm pulses does *E*-SBTub3 isomerize to *Z*-SBTub3 and stop MT polymerization dynamics (10 μM *E*-SBTub3 or *E*-PST-1). (C) Comet count before and after treatment with pre-lit (mostly-*Z*) SBTub3.

(D and E) Data related to Video S1: EB3-GFP-transfected HeLa cells treated with/without SBTub3 were illuminated at 405 nm every 90 s; MT polymerization dynamics were quantified by imaging EB3 comets at 491 nm. (D) EB3 comet counts are reversibly modulated by 405 nm photoactivations with SBTub3 (red) but are unaffected in its absence (blue) (dotted lines indicate 405 nm pulses, n = 5 movies per condition, mean with standard deviation). (E) Representative still images at baseline (t = 0 s); at 10 s/36 s after the first photoactivation (t = 100 s/126 s, comets vanished/recovered); and at 10 s/42 s after the fifth photoactivation (t = 460 s/492 s, comets vanished/recovered). Scale bar, 10 μm.

(legend continued on next page)

40 h later. *Z*-SBTub3's antiproliferative potency in this single-shot experiment (Figure 4A) nearly matched that observed under pulsed re-illuminations every 15 s, indicating the stability of the *Z*-SBTubs in cells in the long term (despite the presence of, e.g., cellular thiols). By comparison, azobenzene-based PST-1 was essentially inactive in this single-shot experiment, which was expected since degradative metabolism as well as thermal relaxation should deplete cellular *Z*-PST levels rapidly (reports suggest within an hour [Sheldon et al., 2016]).

SBTubs Enable Photocontrol of Cellular MT Dynamics Independently of GFP/YFP Imaging

To study SBTubs' ability to effect *in situ* photocontrol of MT dynamics in higher spatiotemporal resolution, we imaged live cells transfected with labeled end binding proteins (EBs). EBs, including EB1 and EB3, mark the GTP cap regions of polymerizing MTs. Imaging fluorescent EB fusion proteins by live-cell confocal microscopy reveals the plus ends of polymerizing MTs as dynamic comets (Merriam et al., 2013; Roostalu et al., 2020), and imaging during photoswitching is a spatiotemporally resolved readout for isomerization-dependent inhibition of MT dynamics by photoswitchable inhibitors (Borowiak et al., 2015; Müller-Deku et al., 2020).

We first tested whether SBTubs avoid any isomerization during imaging, which would make them suitable for fully orthogonal imaging and photocontrol: an important unsolved challenge for intracellular photopharmacology. We imaged MT dynamics using GFP-EB3 with excitation at 488 nm and YFP-EB3 with excitation at 514 nm by confocal microscopy. As hoped from their sharp absorption cutoff above 410 nm, neither GFP nor YFP imaging under treatment with *E*-SBTub3 caused inhibition of MT dynamics; but when 405 nm photoactivation pulses were additionally applied, MT dynamics were rapidly suppressed (Figure 4B). By imaging and photoactivation of cosolvent controls, and imaging under treatment with pre-activated *Z*-SBTub3, we showed that this suppression of MT dynamics is not due to photobleaching but is consistent with selective $E \rightarrow Z$ photoisomerization of SBTub3 under 405 nm only (Figures 4B and 4C). As treatment with *Z*-SBTub3 blocks MT dynamics throughout the imaging time course, this shows that both $E \rightarrow Z$ and $Z \rightarrow E$-SBTub isomerization are fully orthogonal to typical imaging conditions (Figures 4C and S4A–S4C; see discussion in the Supplemental Information). We consider this a powerful demonstration that the SBT scaffold may more generally be well suited for use in photopharmaceuticals, against diverse targets, across many biological systems where GFP and YFP reporters are used.

SBTubs Enable Temporally Reversible MT Photocontrol in Cells that Are Orthogonal to Imaging

Achieving temporally reversible, spatially localized cellular applications of photoactivatable compounds is the major goal of both photopharmacology and photouncaging. These first-generation SBTubs were designed for $E \rightarrow Z$ photoisomerization with high spatiotemporal precision. They cannot be substantially $Z \rightarrow E$ photoisomerized in cells, and they are too stable to undergo substantial spontaneous $Z \rightarrow E$ relaxation at physiological temperatures, so neither process can be relied upon to revert *Z*-SBTub to its bioinactive isomer. However, as in photouncaging, temporally reversible and spatially localized inhibition can still be achieved using spatiotemporally localized activating photoisomerization, if two conditions are met: (1) inhibitor-target dissociation and intracellular or transmembrane diffusion must quickly reduce the concentration of the photoactivated species below its inhibitory threshold and (2) protein function must be immediately restored upon inhibitor dissociation (true for colchicine domain inhibitors). If so, and particularly in systems with a highly nonlinear dose response (such as the MT cytoskeleton), localized photoactivation followed by diffusion-based depletion of the photogenerated bioactive isomer may give complete functional recovery in a single cell or region, on the compound's diffusion or transmembrane partitioning timescale. *Z*-SBTub3 did show fast membrane penetration kinetics, since its addition to cell bath solutions quickly stopped MT dynamics (Figure 4C). We therefore assayed the temporal reversibility of SBTub's cell-localized modulation of MT dynamics by an EB3-GFP imaging assay with pulses of 405 nm photoactivation. MT polymerization dynamics were repeatedly paused then rapidly recovered to normal, with quantifications aligning closely over many cells (Video S1; Figures 4D and 4E).

We performed a similar experiment while changing the cell line, biological label, and fluorescent marker, to test the SBTubs' broader applicability and the hypothesis that SBTubs generate readout in these assays by causatively modulating MT polymerization (rather than, e.g., by directly affecting EB3-GFP/YFP). We repeated the temporal reversibility experiments in A549 lung cancer cell line, transfected with the dsRed-derived tdTomato marker fused to the end binding protein EB1. We observed identical temporal modulation (Figures 4F–4K; Video S2), validated by benchmarking against non-405 nm illuminated cells treated with pre-lit *Z*-SBTub3 (Figures 4F and 4G). Comparing dark and pre-lit SBTub3 with DMSO-only controls and the positive control tubulin inhibitor nocodazole confirmed resistance to both $E \rightarrow Z$ and $Z \rightarrow E$ isomerization during imaging (Figures 4I–4K). SBTub photoswitching can therefore drive highly reproducible, GFP-orthogonal, temporally reversible modulation of MT polymerization in live cells, performance which no other tubulin photopharmaceutical has delivered.

SBTub Photoswitching Permits Subcellularly Resolved MT Inhibition in Primary Neurons

Rapid diffusion of small-molecule inhibitors within cells makes subcellular patterning of photopharmaceuticals against cytosolic

(F–H) Data related to Videos S1 and S2: EB1-tdTomato-transfected A549 cells treated with/without SBTub3 were imaged for EB1 comets at 561 nm. Cells exposed to SBTub3 and pulses of 405 nm show temporally precise suppressions of MT polymerization dynamics upon 405 nm applications that reach maximal inhibition similar to positive controls nocodazole or pre-lit SBTub3, but rapidly recovering to similar levels as non-pulsed SBTub3 or cosolvent controls.
(I–K) Controls related to (B–H). EB3-GFP-transfected HeLa cells were treated with SBTub3, scaffold control SBTub1, or DMSO solvent alone, then imaged directly after treatment, optionally with 405 illuminations interleaved. Movies were analyzed for (I) EB3 comet counts, (J) average EB3 comet density, and (K) average EB3 comet velocity. Data shown as mean ± standard deviation; *p < 0.05, **p < 0.01, ***p < 0.001, ****p < 0.0001; n.s., not significant; n = 10 cells per condition).

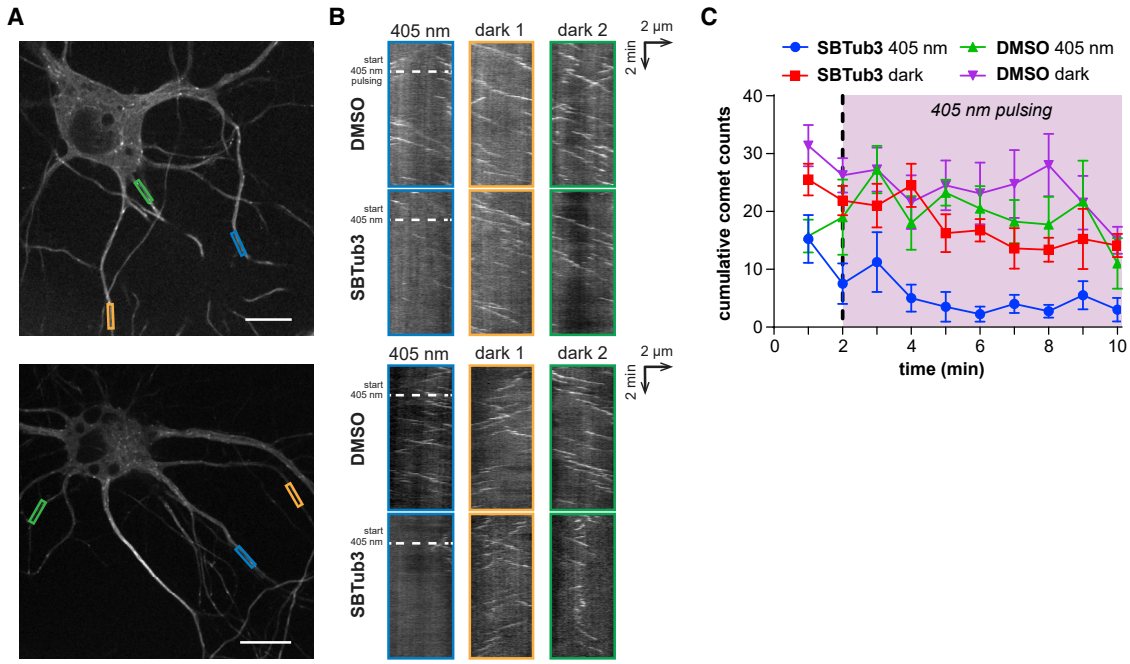

Figure 5. Local SBTub Photoisomerization Inhibits MT Polymerization in Subcellular Regions of Primary Hippocampal Neurons

(A–C) Data related to Video S3: cultured primary neurons (10 days *in vitro*) transfected with EB3-GFP and treated with 1% DMSO were imaged for EB3 for 10 min while an ROI (blue box) was pulsed with 405 nm commencing 2 min into the acquisition (indicated by dotted lines). Baseline EB3 dynamics in the cell and the ROI were shown to be light independent. The same neurons were then exposed to 1 µM SBTub3 and immediately imaged for another 10 min; during this time the same ROI was again pulsed with 405 nm from 2 min onward. (A) Cell images with regions marked, and (B) EB3 kymographs of these regions. The ROI pulsed with 405 nm is boxed in blue; the regions not pulsed with 405 nm are boxed in orange and green. Scale bars, 10 µm. (C) EB3 comet counts accumulated over 20 frame (1 min) intervals (±SEM) plotted over time, for regions treated with or without SBTub3 and 405 nm pulsing (n = 4 cells).

targets challenging. However, large cells (e.g., embryonic systems) or irregularly shaped cells (e.g., neurons) are targets whose geometry and size may favor subcellular patterning. We cultured isolated primary rat hippocampal neurons until neurites developed, then transfected them with EB3-GFP for imaging (Kapitein et al., 2010). For each neuron, we selected several equal-sized areas along independent neurites and monitored the dynamics of EB3 comets before and during SBTub3 treatment, with repetitive ROI-localized 405 nm applications to one of the areas, aiming to locally block MT polymerization in the selected neuronal process area (Figure 5; Video S3). For SBTub3-treated cells, kymographs of 405 nm illuminated neurites showed localized reductions in EB3 comet number and lifetime, while non-illuminated neurites showed no significant changes from baseline; and controls before/after SBTub3 application showed no photobleaching by 405 nm illumination (Figure 5B). Comet counts (Figure 5C) indicated likewise that SBTub3 photoswitching induces subcellularly localized inhibition of MT polymerization.

DISCUSSION

Photopharmacological approaches to high spatiotemporal precision reagents for noninvasive studies of endogenous protein function have made significant progress in the last decade. From original applications in neuroscience (Lester et al., 1980; Volgraf et al., 2005), they now impact membrane and cytoskeleton biology (Borowiak et al., 2015, 2020; Frank et al., 2016; Urban et al., 2018); and recent advances in long-wavelength photoswitches offer prospects for *in vivo* photopharmacology (Bléger et al., 2012; Konrad et al., 2016; Samanta et al., 2013b). However, the scope of targets and assays accessible to photopharmacology has been restricted by its chemistry. The overwhelming majority of photopharmaceutical designs employ azobenzenes as the photoswitch moiety and so inherit their functional limitations: (1) the diazene's nucleophilic and metabolic susceptibility is problematic for addressing intracellular targets or for long-term, systemic *in vivo* applications; (2) its n-π^* absorption in the blue-green spectral region is triggered by imaging standard biological tags (e.g., GFP/YFP); and (3) azobenzenes for cytosolic targets have restricted substituent scope since *ortho*/*para*-electron-donating groups that are key to strong ligand-protein interactions (OH, NH_2, etc.) cause microsecond relaxation rates, so are not bulk photoisomerizable under physiological conditions. Only recently have non-azobenzene photoswitches, such as dithienylethenes and hemithioindigos, been used in bioactive pharmacophores (Sailer et al., 2019; Simeth et al., 2017); and the development of novel photoswitch scaffolds is recognized as a valuable milestone even before reaching cellular applications (Hoorens et al., 2019).

Here, we have demonstrated the design and testing of a novel concept for a GFP-orthogonal metabolically resistant SBT photoswitch scaffold. The SBT scaffold has comparable chemical simplicity with that of azobenzene and delivers spatiotemporally precise photoswitching-based biological control, while also

addressing all three challenges by bringing: (1) biochemical/metabolic robustness; (2) orthogonality to common imaging conditions; and (3) an alternative range of isomerization-tolerant substituents (e.g., including *para*-OH). Thus, SBT expands the scope of intracellular targets and of biological assays (toward *in vivo* use) accessible to photopharmacology.

The reagents conceptually nearest to the SBTubs are the fully photoswitchable (but non-GFP-orthogonal and metabolically labile) PST-1, and (irreversibly) photouncageable inhibitors, such as nitrobenzylether-capped CA4 (Wuhr et al., 2010). A minor issue is that the potency of these SBTubs ($IC_{50} \sim 1$ μM) is less than either previous system (IC_{50} PST-1 ~ 0.5 μM, fully uncaged CA4 ~20 nM); however, further structural tuning of SBTubs may improve potency. It is the different photoresponse of SBTubs that brings them more important advantages and disadvantages. In cells, azobenzenes can undergo $Z \leftrightarrow E$ switching by illumination and $Z \rightarrow E$ isomerization by spontaneous relaxation, whereas this first generation of SBTubs only allows cellular $E \rightarrow Z$ switching (unidirectional activation). Spontaneous $Z \rightarrow E$ relaxation could improve their performance in spatiotemporally localized activation assays, by passively counteracting the build-up of photoactivated but diffused reagent; and bidirectional $Z \leftrightarrow E$ photoswitching would allow active control over the spatiotemporal localization of both *E* and *Z* isomers.

The unidirectional photoactivation of SBTubs is conceptually somewhat similar to that of photouncageable inhibitors; however, their performance differs in five respects (1) typical photocaging groups (e.g., *ortho*-nitrobenzyls) require hydrolysis before cargo release that can take seconds to minutes, which diminishes the spatiotemporal precision of photouncaging (off-to-on) and diffusion (on-to-off). Isomerization, as the SBTs use, is typically orders of magnitude faster (<< ns), and SBTubs give reproducibly high-precision biological control. (2) Photouncaging byproducts are often unspecifically toxic and may also be phototoxic (Klán et al., 2013), while SBTub's photochemically robust $E \rightarrow Z$ isomerization allows cell-tolerated long-term experimentation. (3) Photouncaging strategies add significant molecular weight, which often penalizes bioavailability or biodistribution; they may suffer non-photolytic compound release (enzymatic or spontaneous hydrolysis); and they involve higher synthetic cost (Klán et al., 2013; Reeβing and Szymanski, 2017). SBT inclusion in a pharmacophore does not add compound weight or complexity, and avoids any activation mechanisms except photoactivation. (4) The photocages that are orthogonal to 488 nm imaging (e.g., nitrobenzyls) have low uncaging yield at 405 nm and thus require high photon fluxes to uncage, which can cause phototoxicity problems and also photodegrade the released reagent; whereas SBT can efficiently exploit this common microscopy line with high yield and excellent photostability. (5) Photouncageable probes must be protected from irreversible ambient light-induced photodegradation during synthesis, storage, and use; SBTs are easier to handle and use because accidentally light-exposed stocks can be relaxed quantitatively back to the inactive *E* isomer by warming.

Taken together, these features set SBTs apart from photouncaging approaches and from azobenzene photoswitching, recommending them for reproducible, high-precision, "clean" photopharmacological control particularly in higher-complexity biological systems. We therefore expect that the SBTubs may contribute to high-precision MT cytoskeleton studies and manipulation in neuroscience, motility, and embryology. If SBTubs can also be applied *in vivo* beyond small embryonic systems, it could offer exciting research potential. In larger animals, colchicine domain inhibitors are most often used as vascular disrupting agents and studied *in situ* by microscopy in one- or two-photon mode (Tozer et al., 2001). These are both feasible methods to isomerize SBTubs, and in superficial tissue settings the penetration of UV/violet light can be sufficient for photoswitching (Morstein et al., 2019). So far only one report of systemic pharmacokinetics of a photopharmaceutical has been published (Babii et al., 2020). If SBTubs or their derivatives do have favorable pharmacokinetics, their biochemical stability may enable powerful *in vivo* translation of MT photopharmacology.

We also believe that the development of the SBT scaffold itself is promising for photopharmaceutical development. The SBT scaffold unites photochemical and biochemical robustness with GFP-orthogonality, and tolerates drug-important polar functional groups. These characteristics recommend SBT for research applications that are inaccessible to current photopharmaceuticals, e.g., for intracellular photocontrol in embryos and primary cell isolates of GFP/YFP animal models, both of which are important in development and neurodegeneration. More broadly, it is significant that "scaffold hopping" from azobenzene (PST-1) to SBT (SBTub) has been successful. Novel photoswitches that can substitute typical azobenzenes without requiring total redesign, while offering new performance, are already impacting the hitherto azobenzene-based field of photopharmacology. In this context, diazocines (Reynders et al., 2020; Siewertsen et al., 2009), tetra-*ortho*-substitutions (Bléger et al., 2012), and azoniums (Samanta et al., 2013a) are rapidly garnering applications for spectral shifting. Our work suggests that SBT may be used more generally to substitute azobenzene in photopharmaceutical designs to improve performance on intracellular targets or for optically orthogonal use in live-imaging studies. SBT may thus drive the development of new generations of more powerful photopharmaceuticals against a broader range of biological targets.

SIGNIFICANCE

Photocontrollable reagents have unique potential as high spatiotemporal precision modulators of endogenous biological systems: in particular, systems—such as the microtubule cytoskeleton—where rapid dynamics and tight spatial organization are key to function. Lead compound SBTub3 provides spatiotemporally precise control over endogenous microtubule dynamics in live cells, to a level that has not previously been possible. Subcellularly localized SBTub3 photoswitching can even modulate MT polymerization dynamics in individual neurites: a level of precision manipulation that will motivate a range of highly resolved inhibition studies in neurobiology and beyond. More generally, the practical utility of SBTub3 and of SBT-based photoswitches in biological research is significantly greater than that of previous photopharmaceuticals based on azobenzenes, because the rational design of the SBT photoswitch scaffold solves the three outstanding problems

hampering their biological use. Firstly, photocontrollable inhibitors must be light responsive, but not to the wavelengths used for imaging; the strong isomerization of the azobenzene scaffold under GFP and YFP (even RFP) excitation, can restrict the channels available for imaging and cause significant background activity. Secondly, azobenzenes can be metabolically unstable in the cytosol after illumination, and release intrinsically bioactive products upon degradation. Thirdly, azobenzenes have poor tolerance of key functional groups that drive ligand binding (OH, NH_2, etc.). By contrast, the SBT scaffold's C=C double bond chromophore gives SBT-based photopharmaceuticals (such as SBTub3) outstanding performance in practical biological uses. SBTs are metabolically stable, allowing robust application to cytosolic targets; they tolerate tautomerizable groups without instability of the *cis* isomer; and they are orthogonal to GFP imaging, allowing background-free photoswitching and easy translation between models. Importantly, we show that azobenzene photopharmaceuticals can be redesigned into SBT photopharmaceuticals without losing their mechanism of action or their potency. SBTs are thus a promising advance for high-precision microtubule biology, and for the development of high-performance photopharmaceuticals against other protein targets.

STAR★METHODS

Detailed methods are provided in the online version of this paper and include the following:

SUPPLEMENTAL INFORMATION

Supplemental Information can be found online at https://doi.org/10.1016/j.chembiol.2020.11.007.

ACKNOWLEDGMENTS

This research was supported by funds from the German Research Foundation (DFG: SFB1032 Nanoagents for Spatiotemporal Control project B09 to O.T.-S. and project A08 to T.L.; Emmy Noether grant no. 400324123, SFB TRR 152 project P24 no. 239283807, and SPP 1926 project no. 426018126 to O.T.-S.); the Swiss National Science Foundation (31003A_166608 to M.O.S.); and the Munich Centre for NanoScience initiative (CeNS). J.C.M.M. acknowledges support from an EMBO Long-Term Fellowship. X-ray diffraction data were collected at the beamline X06SA at the Swiss Light Source (Paul Scherrer Institut, Villigen PSI, Switzerland). We thank S. Schmidt (LMU) for help with synthesis; K.T. Wanner (LMU) for collegial discussions; H. Harz, I. Solvei, and C. Jung (LMU microscopy platforms), K. Bartel, A. Vollmar, H. Leonhardt, and S. Zahler (LMU) for access to general biology and microscopy facilities; and D. Hörl (LMU) for measuring microscope laser power. We dedicate this paper to GFP's discoverer Osamu Shimomura,whose devoted research has made modern chemical biology possible.

AUTHOR CONTRIBUTIONS

L.G. performed synthesis, single-photon photocharacterization, *in vitro* studies, figure preparation, coordinated data assembly, and wrote the manuscript. J.C.M.M. performed characterization of EB3 dynamics, temporally reversible live-cell imaging studies, and subcellularly localized photoswitching. Y.K. performed *in vitro* studies. M.W. performed tubulin protein production, purification, crystallization, crystal handling, and X-ray data collection, processing, and refinement. T.W. performed tubulin crystal handling, data collection, and data processing and refinement. S.D.P. performed two-photon photocharacterization. R.B. performed cell-free tubulin polymerization assays. E.N. performed live-cell imaging on A549 cell lines. K.I.J. and L.C.K. performed primary neuron isolation and culture. N.O. performed tubulin protein production, purification, and crystallization. T.L. supervised two-photon photocharacterization. J.S. and M.O.S. supervised protein crystallography. A.A. supervised characterization of EB3 dynamics, temporally reversible cell imaging and subcellularly localized photoswitching. J.A. performed *in vitro* studies, coordinated data assembly and figure preparation, and supervised all other cell biology. O.T.-S. designed the concept and experiments, supervised all other experiments, coordinated data assembly, and wrote the manuscript with input from all authors.

DECLARATION OF INTERESTS

The authors declare no competing interests.

Received: October 21, 2020
Revised: November 10, 2020
Accepted: November 13, 2020
Published: February 18, 2021

REFERENCES

Adams, P.D., Afonine, P.V., Bunkoczi, G., Chen, V.B., Davis, I.W., Echols, N., Headd, J.J., Hung, L.-W., Kapral, G.J., Grosse-Kunstleve, R.W., et al. (2010). PHENIX: a comprehensive Python-based system for macromolecular structure solution. Acta Crystallogr. Section D *66*, 213–221.

Awad, M.K., El-Hendawy, M.M., Fayed, T.A., Etaiw, S.E.H., and English, N.J. (2013). Aromatic ring size effects on the photophysics and photochemistry of styrylbenzothiazole. Photochem. Photobiol. Sci. *12*, 1220–1231.

Babii, O., Afonin, S., Schober, T., Garmanchuk, L.V., Ostapchenko, L.I., Yurchenko, V., Zozulya, S., Tarasov, O., Pishel, I., Ulrich, A.S., et al. (2020). Peptide drugs for photopharmacology: how much of a safety advantage can be gained by photocontrol? Future Drug Discov. *2*, FDD28.

Baell, J.B., and Nissink, J.W.M. (2018). Seven year itch: pan-assay interference compounds (PAINS) in 2017—utility and limitations. ACS Chem. Biol. *13*, 36–44.

Berdnikova, D., Fedorova, O., Gulakova, E., and Ihmels, H. (2012). Photoinduced in situ generation of a DNA-binding benzothiazoloquinolinium derivative. Chem. Commun. *48*, 4603–4605.

Bléger, D., Schwarz, J., Brouwer, A.M., and Hecht, S. (2012). o-Fluoroazobenzenes as readily synthesized photoswitches offering nearly quantitative two-way isomerization with visible light. J. Am. Chem. Soc. *134*, 20597–20600.

Borowiak, M., Küllmer, F., Gegenfurtner, F., Peil, S., Nasufovic, V., Zahler, S., Thorn-Seshold, O., Trauner, D., and Arndt, H.-D. (2020). Optical manipulation of F-actin with photoswitchable small molecules. J. Am. Chem. Soc. *142*, 9240–9249.

Borowiak, M., Nahaboo, W., Reynders, M., Nekolla, K., Jalinot, P., Hasserodt, J., Rehberg, M., Delattre, M., Zahler, S., Vollmar, A., et al. (2015). Photoswitchable inhibitors of microtubule dynamics optically control mitosis and cell death. Cell *162*, 403–411.

Boulègue, C., Löweneck, M., Renner, C., and Moroder, L. (2007). Redox potential of azobenzene as an amino acid residue in peptides. ChemBioChem *8*, 591–594.

Broichhagen, J., Frank, J.A., and Trauner, D. (2015). A roadmap to success in photopharmacology. Acc. Chem. Res. *48*, 1947–1960.

Castle, B.T., and Odde, D.J. (2015). Optical control of microtubule dynamics in time and space. Cell *162*, 243–245.

Dumontet, C., and Jordan, M.A. (2010). Microtubule-binding agents: a dynamic field of cancer therapeutics. Nat. Rev. Drug Discov. *9*, 897.

Eguchi, K., Taoufiq, Z., Thorn-Seshold, O., Trauner, D., Hasegawa, M., and Takahashi, T. (2017). Wild-type monomeric α-synuclein can impair vesicle endocytosis and synaptic fidelity via tubulin polymerization at the calyx of Held. J. Neurosci. *37*, 6043–6052.

El-Hendawy, M.M., Fayed, T.A., Awad, M.K., English, N.J., Etaiw, S.E.H., and Zaki, A.B. (2015). Photophysics, photochemistry and thermal stability of diarylethene-containing benzothiazolium species. J. Photochem. Photobiol. *301*, 20–31.

Emsley, P., and Cowtan, K. (2004). Coot: model-building tools for molecular graphics. Acta Crystallogr. Section D *60*, 2126–2132.

Engdahl, A.J., Torres, E.A., Lock, S.E., Engdahl, T.B., Mertz, P.S., and Streu, C.N. (2015). Synthesis, characterization, and bioactivity of the photoisomerizable tubulin polymerization inhibitor azo-combretastatin A4. Org. Lett. *17*, 4546–4549.

Francioso, A., Boffi, A., Villani, C., Manzi, L., D'Erme, M., Macone, A., and Mosca, L. (2014). Isolation and identification of 2,4,6-trihydroxyphenanthrene as a byproduct of trans-resveratrol photochemical isomerization and electrocyclization. J. Org. Chem. *79*, 9381–9384.

Frank, J.A., Franquelim, H.G., Schwille, P., and Trauner, D. (2016). Optical control of lipid rafts with photoswitchable ceramides. J. Am. Chem. Soc. *138*, 12981–12986.

Gaspari, R., Prota, A.E., Bargsten, K., Cavalli, A., and Steinmetz, M.O. (2017). Structural basis of *cis*- and *trans*-combretastatin binding to tubulin. Chem *2*, 102–113.

Hofmann, A.W. (1880). Zimmtsäurederivat des Amidophenylmercaptans. Chem. Ber. 1235–1238.

Hoorens, M.W.H., Medved', M., Laurent, A.D., Di Donato, M., Fanetti, S., Slappendel, L., Hilbers, M., Feringa, B.L., Jan Buma, W., and Szymanski, W. (2019). Iminothioindoxyl as a molecular photoswitch with 100 nm band separation in the visible range. Nat. Comm. *10*, 2390.

Horspool, W.M., and Lenci, F. (2004). CRC Handbook of Organic Photochemistry and Photobiology, 2nd ed. edn (CRC Press).

Hüll, K., Morstein, J., and Trauner, D. (2018). In vivo photopharmacology. Chem. Rev. *118*, 10710–10747.

Janke, C., and Steinmetz, M.O. (2015). Optochemistry to control the microtubule cytoskeleton. EMBO J. *34*, 2114–2116.

Kabsch, W. (2010). XDS. Acta Crystallographica Section D, Biol. Crystallogr. *66*, 125–132.

Kapitein, L.C., Yau, K.W., and Hoogenraad, C.C. (2010). Chapter 7. Microtubule dynamics in dendritic spines. In Methods in Cell Biology, L. Cassimeris and P. Tran, eds. (Academic Press), pp. 111–132.

Klán, P., Šolomek, T., Bochet, C.G., Blanc, A., Givens, R., Rubina, M., Popik, V., Kostikov, A., and Wirz, J. (2013). Photoremovable protecting groups in chemistry and biology: reaction mechanisms and efficacy. Chem. Rev. *113*, 119–191.

Kleele, T., Marinković, P., Williams, P.R., Stern, S., Weigand, E.E., Engerer, P., Naumann, R., Hartmann, J., Karl, R.M., Bradke, F., et al. (2014). An assay to image neuronal microtubule dynamics in mice. Nat. Commun. *5*, 4827.

Konrad, D.B., Frank, J.A., and Trauner, D. (2016). Synthesis of redshifted azobenzene photoswitches by late-stage functionalization. Chem. Eur. J. *22*, 4364–4368.

La Sala, G., Olieric, N., Sharma, A., Viti, F., de Asis Balaguer Perez, F., Huang, L., Tonra, J.R., Lloyd, G.K., Decherchi, S., Díaz, J.F., et al. (2019). Structure, thermodynamics, and kinetics of plinabulin binding to two tubulin isotypes. Chem *5*, 2969–2986.

Lei, H., Mo, M., He, Y., Wu, Y., Zhu, W., and Wu, L. (2019). Bioactivatable reductive cleavage of azobenzene for controlling functional dumbbell oligodeoxynucleotides. Bioorg. Chem. *91*, 103106.

Lester, H.A., Krouse, M.E., Nass, M.M., Wassermann, N.H., and Erlanger, B.F. (1980). A covalently bound photoisomerizable agonist: comparison with reversibly bound agonists at electrophorus electroplaques. J. Gen. Physiol. *75*, 207–232.

Lin, C.M., Singh, S.B., Chu, P.S., Dempcy, R.O., Schmidt, J.M., Pettit, G.R., and Hamel, E. (1988). Interactions of tubulin with potent natural and synthetic analogs of the antimitotic agent combretastatin: a structure-activity study. Mol. Pharmacol. *34*, 200–208.

Meijering, E., Dzyubachyk, O., and Smal, I. (2012). Chapter 9. Methods for cell and particle tracking. In Methods in Enzymology, P.M. conn, ed. (Academic Press), pp. 183–200.

Merriam, E.B., Millette, M., Lumbard, D.C., Saengsawang, W., Fothergill, T., Hu, X., Ferhat, L., and Dent, E.W. (2013). Synaptic regulation of microtubule dynamics in dendritic spines by calcium, F-actin, and drebrin. J. Neurosci. *33*, 16471.

Mishra, A., Thangamani, A., Chatterjee, S., Chipem, F.A.S., and Krishnamoorthy, G. (2013). Photoisomerization of *trans*-2-[*4*'-(dimethylamino)styryl]benzothiazole. Photochem. Photobiol. *89*, 247–252.

Moreno, J., Gerecke, M., Dobryakov, A.L., Ioffe, I.N., Granovsky, A.A., Bléger, D., Hecht, S., and Kovalenko, S.A. (2015). Two-photon-induced versus one-photon-induced isomerization dynamics of a bistable azobenzene derivative in solution. J. Phys. Chem. B *119*, 12281–12288.

Morstein, J., Hill, R.Z., Novak, A.J.E., Feng, S., Norman, D.D., Donthamsetti, P.C., Frank, J.A., Harayama, T., Williams, B.M., Parrill, A.L., et al. (2019). Optical control of sphingosine-1-phosphate formation and function. Nat. Chem. Biol. *15*, 623–631.

Müller-Deku, A., Meiring, J.C.M., Loy, K., Kraus, Y., Heise, C., Bingham, R., Jansen, K.I., Qu, X., Bartolini, F., Kapitein, L.C., et al. (2020). Photoswitchable paclitaxel-based microtubule stabilisers allow optical control over the microtubule cytoskeleton. Nat Commun *11*, 4640.

Pecqueur, L., Duellberg, C., Dreier, B., Jiang, Q., Wang, C., Plückthun, A., Surrey, T., Gigant, B., and Knossow, M. (2012). A designed ankyrin repeat protein selected to bind to tubulin caps the microtubule plus end. Proc. Natl. Acad. Sci. U S A *109*, 12011.

Peterson, J.R., and Mitchison, T.J. (2002). Small molecules, big impact. Chem. Biol. *9*, 1275–1285.

Reeßing, F., and Szymanski, W. (2017). Beyond photodynamic therapy: light-activated cancer chemotherapy. Curr. Med. Chem. *24*, 4905–4950.

Reynders, M., Matsuura, B.S., Bérouti, M., Simoneschi, D., Marzio, A., Pagano, M., and Trauner, D. (2020). PHOTACs enable optical control of protein degradation. Sci. Adv. *6*, eaay5064.

Roostalu, J., Thomas, C., Cade, N.I., Kunzelmann, S., Taylor, I.A., and Surrey, T. (2020). The speed of GTP hydrolysis determines GTP cap size and controls microtubule stability. eLife *9*, e51992.

Sailer, A., Ermer, F., Kraus, Y., Bingham, R., Lutter, F.H., Ahlfeld, J., and Thorn-Seshold, O. (2020). Potent hemithioindigo-based antimitotics photocontrol the microtubule cytoskeleton in cellulo. Beilstein J. Org. Chem. *16*, 125–134.

Sailer, A., Ermer, F., Kraus, Y., Lutter, F., Donau, C., Bremerich, M., Ahlfeld, J., and Thorn-Seshold, O. (2019). Hemithioindigos for cellular photopharmacology: desymmetrised molecular switch scaffolds enabling design control over the isomer-dependency of potent antimitotic bioactivity. ChemBioChem *20*, 1305–1314.

Samanta, S., Babalhavaeji, A., Dong, M.-x., and Woolley, G.A. (2013a). Photoswitching of ortho-substituted azonium ions by red light in whole blood. Angew. Chem. Int. Ed. *52*, 14127–14130.

Samanta, S., Beharry, A.A., Sadovski, O., McCormick, T.M., Babalhavaeji, A., Tropepe, V., and Woolley, G.A. (2013b). Photoswitching azo compounds in vivo with red light. J. Am. Chem. Soc. *135*, 9777–9784.

Schehr, M., Ianes, C., Weisner, J., Heintze, L., Müller, M.P., Pichlo, C., Charl, J., Brunstein, E., Ewert, J., Lehr, M., et al. (2019). 2-Azo-, 2-diazocine-thiazols and 2-azo-imidazoles as photoswitchable kinase inhibitors: limitations and pitfalls of the photoswitchable inhibitor approach. Photochemical Photobiological Sci. *18*, 1398–1407.

Schindelin, J., Arganda-Carreras, I., Frise, E., Kaynig, V., Longair, M., Pietzsch, T., Preibisch, S., Rueden, C., Saalfeld, S., Schmid, B., et al. (2012). Fiji: an open-source platform for biological-image analysis. Nat. Methods *9*, 676–682.

Shan, Y.S., Zhang, J., Liu, Z., Wang, M., and Dong, Y. (2011). Developments of combretastatin A-4 derivatives as anticancer agents. Curr. Med. Chem. *18*, 523–538.

Sheldon, J.E., Dcona, M.M., Lyons, C.E., Hackett, J.C., and Hartman, M.C.T. (2016). Photoswitchable anticancer activity via *trans-cis* isomerization of a combretastatin A-4 analog. Org. Biomol. Chem. *14*, 40–49.

Siewertsen, R., Neumann, H., Buchheim-Stehn, B., Herges, R., Näther, C., Renth, F., and Temps, F. (2009). Highly efficient reversible Z-E photoisomerization of a bridged azobenzene with visible light through resolved S1($n\pi^*$) absorption bands. J. Am. Chem. Soc. *131*, 15594–15595.

Simeth, N.A., Kneuttinger, A.C., Sterner, R., and König, B. (2017). Photochromic coenzyme Q derivatives: switching redox potentials with light. Chem. Sci. *8*, 6474–6483.

Singh, A., Saha, T., Begemann, I., Ricker, A., Nüsse, H., Thorn-Seshold, O., Klingauf, J., Galic, M., and Matis, M. (2018). Polarized microtubule dynamics directs cell mechanics and coordinates forces during epithelial morphogenesis. Nat. Cell Biol *20*, 1126–1133.

Smart, O.S., Womack, T.O., Flensburg, C., Keller, P., Paciorek, W., Sharff, A., Vonrhein, C., and Bricogne, G. (2012). Exploiting structure similarity in refinement: automated NCS and target-structure restraints in BUSTER. Acta Cryst. D *68*, 368–380.

Stepanova, T., Slemmer, J., Hoogenraad, C.C., Lansbergen, G., Dortland, B., De Zeeuw, C.I., Grosveld, F., van Cappellen, G., Akhmanova, A., and Galjart, N. (2003). Visualization of microtubule growth in cultured neurons via the use of eb3-GFP (end-binding protein 3-green fluorescent protein). J. Neurosci. *23*, 2655–2664.

Strzyz, P.J., Lee, H.O., Sidhaye, J., Weber, I.P., Leung, L.C., and Norden, C. (2015). Interkinetic nuclear migration is centrosome independent and ensures apical cell division to maintain tissue integrity. Dev. Cell *32*, 203–219.

Tickle, I.J., Flensburg, C., Keller, P., Paciorek, W., Sharff, A., Smart, O., Vonrhein, C., and Bricogne, G. (2018). STARANISO Anisotropy and Bayesian Estimation Server (Global Phasing Ltd).

Tseng, Q., Duchemin-Pelletier, E., Deshiere, A., Balland, M., Guillou, H., Filhol, O., and Thery, M. (2012). Spatial organization of the extracellular matrix regulates cell-cell junction positioning. Proc. Natl. Acad. Sci. U S A *109*, 1506–1511.

Tozer, G.M., Prise, V.E., Wilson, J., Cemazar, M., Shan, S., Dewhirst, M.W., Barber, P.R., Vojnovic, B., and Chaplin, D.J. (2001). Mechanisms associated with tumor vascular shut-down induced by combretastatin A-4 phosphate: intravital microscopy and measurement of vascular permeability. Cancer Res. *61*, 6413–6422.

Tron, G.C., Pirali, T., Sorba, G., Pagliai, F., Busacca, S., and Genazzani, A.A. (2006). Medicinal chemistry of combretastatin A4: present and future directions. J. Med. Chem. *49*, 3033–3044.

Urban, P., Pritzl, S.D., Konrad, D.B., Frank, J.A., Pernpeintner, C., Roeske, C.R., Trauner, D., and Lohmüller, T. (2018). Light-controlled lipid interaction and membrane organization in photolipid bilayer vesicles. Langmuir *34*, 13368–13374.

Vandestadt, C., Vanwalleghem, G.C., Castillo, H.A., Li, M., Schulze, K., Khabooshan, M., Don, E., Anko, M.-L., Scott, E.K., and Kaslin, J. (2019). Early migration of precursor neurons initiates cellular and functional regeneration after spinal cord injury in zebrafish. bioRxiv, 539940.

Volgraf, M., Gorostiza, P., Numano, R., Kramer, R.H., Isacoff, E.Y., and Trauner, D. (2005). Allosteric control of an ionotropic glutamate receptor with an optical switch. Nat. Chem. Biol. *2*, 47.

Weinert, T., Olieric, N., Cheng, R., Brünle, S., James, D., Ozerov, D., Gashi, D., Vera, L., Marsh, M., Jaeger, K., et al. (2017). Serial millisecond crystallography for routine room-temperature structure determination at synchrotrons. Nat. Commun. *8*, 542.

Wittmann, T., Dema, A., and van Haren, J. (2020). Lights, cytoskeleton, action: optogenetic control of cell dynamics. Curr. Opin. Cell Biol. *66*, 1–10.

Wuhr, M., Tan, E.S., Parker, S.K., Detrich, H.W., 3rd, and Mitchison, T.J. (2010). A model for cleavage plane determination in early amphibian and fish embryos. Curr. Biol. *20*, 2040–2045.

Zenker, J., White, M.D., Gasnier, M., Alvarez, Y.D., Lim, H.Y.G., Bissiere, S., Biro, M., and Plachta, N. (2018). Expanding actin rings zipper the mouse embryo for blastocyst formation. Cell *173*, 776–791.

Zenker, J., White, M.D., Templin, R.M., Parton, R.G., Thorn-Seshold, O., Bissiere, S., and Plachta, N. (2017). A microtubule-organizing center directing intracellular transport in the early mouse embryo. Science *357*, 925–928.

STAR★METHODS

KEY RESOURCES TABLE

REAGENT or RESOURCE	SOURCE	IDENTIFIER
Antibodies		
rabbit α-tubulin primary antibody	Abcam	Cat#ab18251; RRID: AB_2210057
goat-anti-rabbit Alexa fluor 488 secondary antibody	Abcam	Cat#ab150077, RRID: AB_2630356
Chemicals, Peptides, and Recombinant Proteins		
SBTub1	this paper	N/A
SBTub2	this paper	N/A
SBTub3	this paper	N/A
SBTub4	this paper	N/A
PST-1	Borowiak et al., 2015	N/A
Glutathione (GSH)	TCI	Cat#G0073; CAS:27025-41-8
99% tubulin (porcine brain)	Cytoskeleton Inc.	Cat#T240
tubulin (bovine brain)	Centro de Investigaciones Biológicas (Microtubule Stabilizing Agents Group), CSIC, Madrid, Spain	N/A
Human liver microsomes	XenoTech	Cat#H0630 lot#1610016
Critical Commercial Assays		
Vivid™ CYP450 Screening Kit	Thermo Fisher Scientific	Cat#P2871, P3027, P2980, P2954
Predictor™ hERG Fluorescence Polarization Assay	Invitrogen/ Thermo Fisher Scientific	Cat#PV5365
Deposited Data		
tubulin-DARPin D1-*Z*-**SBTub2**	this paper	6ZWC
tubulin-DARPin D1-*Z*-**SBTub3**	this paper	6ZWB
Tubulin Darpin room-temperature structure	Weinert et al., 2017	5NQT
Tubulin-Combretastatin A4 complex	Gaspari et al., 2017	5LYJ
Experimental Models: Cell Lines		
HeLa cell line	DSMZ (German Collection of Microorganisms and Cell Cultures)	ACC 57d
A549 cell line	ATCC	CCL-185
Experimental Models: Organisms/Strains		
Rattus norvegicus (Wistar; HanRj:WI)	RGD, Janvier labs	Cat# 13792727; RRID: RGD_13792727
Recombinant DNA		
EB3-GFP (used with neurons)	Stepanova et al., 2003	N/A
EB3-GFP (used with HeLa cells)	Strzyz et al., 2015	Addgene Plasmid #105948; RRID: Addgene_105948
EB3-YFP	Kleele et al., 2014	N/A
EB1-tdTomato	Dent et al., unpublished	Addgene Plasmid #50825; RRID:Addgene_50825
Software and Algorithms		
Fiji (ImageJ)	Schindelin et al., 2012	https://imagej.net/Fiji
ComDet plugin to ImageJ	E. Katrukha, University of Utrecht	https://github.com/ekatrukha/ComDet
MTrackJ plugin to ImageJ	Meijering et al., 2012	https://imagescience.org/meijering/software/mtrackj/

(*Continued on next page*)

Continued

REAGENT or RESOURCE	SOURCE	IDENTIFIER
Template Matching plugin in ImageJ	Tseng et al., 2012	https://sites.google.com/site/qingzongtseng/template-matching-ij-plugin
"Flowing" FACS analysis software	P. Terho, Turku Centre for Biotechnology	https://bioscience.fi/services/cell-imaging/flowing-software/
X-ray: Data processing (XDS)	Kabsch, 2010	http://xds.mpimf-heidelberg.mpg.de/
X-ray: Data correction (Staraniso)	Tickle et al., 2018	http://staraniso.globalphasing.org/
X-ray: ligands and restraints (Grade server)	Smart et al., 2012	http://grade.globalphasing.org
X-ray: refinement (PHENIX)	Adams et al., 2010	https://www.phenix-online.org/download/
X-ray: refinement (COOT)	Emsley and Cowtan, 2004	https://www2.mrc-lmb.cam.ac.uk/personal/pemsley/coot/

RESOURCE AVAILABILITY

Lead Contact

Requests for further information and requests for reagents and resources should be directed to and will be fulfilled by Lead Contact, Oliver Thorn-Seshold (oliver.thorn-seshold@cup.lmu.de).

Materials Availability

All unique reagents generated in this study are available from the Lead Contact without restriction for non-commercial applications, or with a completed Materials Transfer Agreement if there is potential for commercial applications; requestors are required to handle all shipping and customs costs.

Data and Code Availability

The X-Ray datasets generated are available at the Protein Data Bank as tubulin-DARPin D1-*Z*-**SBTub2** (PDB 6ZWC) and tubulin-DARPin D1-*Z*-**SBTub3** (PDB 6ZWB).

EXPERIMENTAL MODEL AND SUBJECT DETAILS

HeLa Human Cervical Carcinoma Cells

HeLa human cervical carcinoma cells (female) were maintained in Dulbecco's modified Eagle's medium (DMEM, PAN-Biotech) supplemented with 10% fetal calf serum (FCS), 100 U/mL penicillin and 100 U/mL streptomycin, at 37°C in a 5% CO_2 atmosphere. Cell line was last authenticated via STR-typing by the distributer (DSMZ (German Collection of Microorganisms and Cell Cultures) and ATCC) and are regularly replaced with new working stocks from our master cell bank.

A549 Human Lung Cancer Cells

A549 human lung cancer cells (male) were maintained in Dulbecco's modified Eagle's medium (DMEM, PAN-Biotech) supplemented with 10% fetal calf serum (FCS), 100 U/mL penicillin and 100 U/mL streptomycin, at 37°C in a 5% CO_2 atmosphere. Cell line was last authenticated via STR-typing by the distributer (DSMZ (German Collection of Microorganisms and Cell Cultures) and ATCC) and are regularly replaced with new working stocks from our master cell bank.

Rat Primary Hippocampal Neurons

All animal experiments were performed in accordance with Dutch law (Wet op de Dierproeven, 1996) and European regulations (Directive 2010/63/EU) under animal licence AVD1080020173404. All animal experiments were approved by the Dutch Animal Experiments Committee (DEC, Dier Experimenten Commissie) and were in line with the institutional guidelines of Utrecht University. Primary hippocampal neurons were derived from hippocampi of embryonic day 18 pups (male and female) from pregnant Wistar rats (Janvier; at least 10 weeks of age and not involved in any previous experiments).

Mouse Hepatic Microsomes

Mouse hepatic microsomes were isolated from pooled, perfused livers of male Balb/c mice (n=50) by Bienta Biology Services (Kiev, Ukraine) under the ethics guidelines of Enamine/Bienta.

Human Hepatic Microsomes

Human hepatic microsomes were purchased from XenoTech (Cat#H0630, lot#1610016, n=50), no available information how samples were allocated to experimental groups.

Transfection

Transient transfections were performed with *EB3-GFP* (Stepanova et al., 2003; Strzyz et al., 2015), *EB3*-YFP (Kleele et al., 2014). or *EB1-tdTomato* plasmids using jetPRIME (Polyplus), FuGENE 6 (Promega) or Lipofectamine 2000 (Invitrogen) reagents according to the manufacturers' instructions and cells were imaged 24 h later (HeLa, A549) or 3 days later (neurons).

METHODS DETAILS

Compound Synthesis and Characterisation

All reactions and characterisations were performed with unpurified, undried, non-degassed solvents and reagents from commercial suppliers (Sigma-Aldrich, TCI Europe N.V., Fisher Scientific etc.), used as obtained, under closed air atmosphere without special precautions. Manual flash column chromatography was performed on Merck silica gel Si-60 (40–63 μm). MPLC flash column chromatography performed on a Biotage Isolera Spektra system, using Biotage prepacked silica cartridges. Thin-layer chromatography (TLC) was run on 0.25 mm Merck silica gel plates (60, F-254), with UV light (254 nm and 365 nm) as visualizing agents. NMR characterisation was performed on a Bruker Ascend 400 (400 MHz & 100 MHz for ^{1}H and ^{13}C respectively). HRMS was carried out by the Zentrale Analytik of the LMU Munich. Analytical HPLC-MS was performed on an Agilent 1100 SL coupled HPLC-MS system with H_2O:MeCN eluent gradients through a Thermo Scientific Hypersil GOLD™ C18 column (1.9 μm; 3 × 50 mm) maintained at 25°C, detected on an Agilent 1100 series diode array detector and a Bruker Daltonics HCT-Ultra spectrometer (ESI mode, unit m/z). IR spectra were recorded on a PerkinElmer Spectrum BX II FT-IR system. Full experimental details are given in the Data S1 Part C.

Photocharacterisation

UV-Vis absorption spectra measurements in cuvette were acquired on an Agilent CaryScan 60 (1 cm pathlength) at room temperature (25°C) with default compound concentrations of 25 μM and default solvents of PBS at pH ~7.4 with 10 % of DMSO as cosolvent. "Star" LEDs (H2A1-models spanning 360–435 nm Roithner Lasertechnik; FWHM ~25 nm and 260 nm HP-LED Sahlmann Photochemical Solutions) were used for photoisomerisations in cuvette that were also predictive of what would be obtained in LED-illuminated cell culture. Spectra of pure *E* and *Z* isomers were acquired from the HPLC's inline Agilent 1100 series diode array detector (DAD) over the range 200–550 nm, manually baselining across each elution peak of interest to correct for eluent composition. Two-photon excitation was performed using a mode-locked Ti-Sapphire Laser operating at 780 nm (Spectra Physics, Tsunami) with a pulse repetition frequency of 80 MHz (pulse with <100 fs) and an output power of 0.65 W, coupled into an upright Zeiss Axiotech 100 microscope and focused with a 40× reflective objective (Thorlabs, LMM-40X-UVV, measuring sample transmittance using a HAL 100 illuminator (Carl Zeiss) and a SP300i spectrograph equipped with a MicroMAX CCD camera for signal recording (both Princeton Instruments), between 360 nm and 380 nm. For more information on *in vitro* photocharacterization see Data S1 Part D

Stability towards Glutathione (GSH)

Samples of both all-*E* ("dark") and mostly-*Z* ("pre-lit") **SBTub2** and **PST-1** were prepared in PBS pH ~7.4 with 10% DMSO, containing GSH (10 mM), in UV-Vis cuvettes that were sealed under air atmosphere (gas head volume <2 mL) with parafilm and maintained at 37°C, during absorbance measurements over several hours in a Agilent Cary 60 spectrophotometer. "Dark" assays were performed with the *E*-isomers of the test compounds; "pre-lit" **SBTub2** had been pre-illuminated to reach PSS under 360 nm light; while "lit" **PST-1** was maintained under continuous illumination from above with a 390 nm LED to maintain **PST-1** in a mostly-*cis* state. **SBTub2** was monitored at 345 nm, while **PST-1** was monitored at 378 nm and 440 nm for dark and lit states, respectively. For detailed experimental procedure and discussion on the GSH stability of **SBTub2** and **PST-1** see Data S1 Part E.

Microsomal Stability, CYP Inhibition and hERG Inhibition

SBTubs' stability to degradation by liver microsomes was assessed by *in vitro* studies using isolated mouse and human liver microsomes, performed by Bienta Biology Services (Kiev, Ukraine) over a 40 min timecourse at 37°C following standard practice. Mouse hepatic microsomes were isolated from pooled, perfused livers of male Balb/c mice (n=50); human hepatic microsomes were supplied by XenoTech. Microsomal incubations were performed in duplicates and control incubations were performed replacing the NADPH-cofactor system with PBS. Supernatants were analyzed using HPLC-MS. The potential for CYP450 inhibition was assessed by *in vitro* inhibition studies using fluorogenic CYP450 substrates with the corresponding CYP450 enzymes and NADPH regeneration system (Vivid CYP450 Screening Kits) performed by Bienta Biology Services. hERG inhibition experiments were performed by Bienta Biology Services using Invitrogen PredictorTM hERG Fluorescence Polarization Assay in accordance with the manufacturer's protocol (Protocol PV5365). Please see Data S1 Part E for more information.

Tubulin Polymerisation *In Vitro*

99% purity tubulin from porcine brain was obtained from Cytoskeleton Inc. (cat. #T240) and polymerisation assays run according to manufacturer's instructions. Tubulin was pre-incubated for 10 min at 37°C with "lit"- (after 360 nm illumination) or "dark" (all-*E* conditions) **SBTub** (20 μM) in buffer (with 3% DMSO, 10% glycerol); at time zero, GTP (1 mM) was added and the change in absorbance at 340 nm was monitored over 15 mins at 37°C (Lin et al., 1988).

Protein Production, Crystallisation and Soaking

The DARPin D1 was prepared as previously described (Pecqueur et al., 2012). Tubulin from bovine brain was purchased from the Centro de Investigaciones Biológicas (Microtubule Stabilizing Agents Group), CSIC, Madrid, Spain. The tubulin-DARPin D1 (TD1; (La Sala et al., 2019; Pecqueur et al., 2012; Weinert et al., 2017)) complex was formed by mixing the respective components in a 1:1.1 molar ratio. The TD1 complex was crystallised overnight by the hanging drop vapor diffusion method (drop size 2 μL, drop ratio 1:1) at a concentration of 15.9 mg/mL and at 20°C with a precipitant solution containing 18% PEG 3350, 0.2 M ammonium sulfate and 0.1 M bis-tris methane, pH 5.5. All drops were subsequently hair-seeded with crystalline material obtained in previous PEG-screening, which resulted in single and large (0.5 μm) TD1 complex crystals. The crystals were fished and transferred into new precipitant solution drops containing 10% DMSO and compounds (*E*-**SBTub2**/*E*-**SBTub3**) at final concentrations 2 mM, then 360 nm LED illumination was applied for 5 min to generate *Z*-**SBTub**s *in situ*. After 4 h of soaking in the dark, the crystals were mounted for X-ray diffraction data collection.

X-ray Diffraction Data Collection, Processing and Refinement

Data were collected at beamline X06SA at the Swiss Light Source (Paul Scherrer Institute, Villigen, Switzerland). The beam was focused to 30 × 30 μm, the flux was 3 × 10^{10} photons/s and the data collection speed was 2°/s at an oscillation range of 0.2° per frame (see Table S1). For TD1-**SBTub2** and TD1-**SBTub3**, 210° and 220° of data were collected, respectively. Data processing was done with XDS (Kabsch, 2010). Due to anisotropy, the data were corrected using the Staraniso server (Tickle et al., 2018) (http://staraniso.globalphasing.org/). The structures were solved by molecular replacement using PDB ID 5NQT as a search model (Weinert et al., 2017). The ligands and restraints were generated with the grade server (Smart et al., 2012) (http://grade.globalphasing.org/) using their SMILES annotation. The structures were then refined iteratively in PHENIX (Adams et al., 2010) with manual editing cycles in COOT (Emsley and Cowtan, 2004). For more information please see Data S1 Part F

MTT Antiproliferation Assay

Cells seeded in 96-well plates at 5,000 cells/well and left to adhere for 24 h were treated with *E*-**SBTub**s under the indicated lighting conditions for 48 h (1% DMSO; six technical replicates). Compounds and cosolvent were added *via* a D300e digital dispenser (Tecan) and cells were either incubated under "dark" (light-excluded) or "lit" conditions (where pulsed illuminations were applied by multi-LED arrays to create and maintain the wavelength-dependent photostationary state isomer ratios throughout the experiment, as previously described (Borowiak et al., 2015)). Cells were then treated with 0.5 mg/mL (3-(4,5-dimethylthiazol-2-yl)-2,5-diphenyl tetrazolium bromide (MTT) for 3 h; the medium was aspirated and formazan crystals were re-dissolved in DMSO (100 μL) before measuring absorbance at 550 nm using a FLUOstar Omega microplate reader (BMG Labtech). Absorbance was averaged over the technical replicates, and normalised as viability by reference to the cosolvent-only control (set as 100%) and to zero absorbance (set as 0%).

Cell Cycle Analysis

E-**SBTub**s were added to HeLa cells in 24-well plates (seeding density: 50,000 cells/well) and incubated under "dark" or "lit" conditions for 24 h. Cells were collected, permeabilised and stained with 2 μg/mL propidium iodide (PI) at 4°C for 30 min. Following PI staining, cells were analysed by flow cytometry using a FACS Canto II flow cytometer (Becton Dickinson) run by BD FACSDiva software. 30,000 cells were measured per condition and the data were transferred to *Flowing* software for cell cycle analysis. Cells were sorted into sub-G1, G1, S and G_2/M phase according to DNA content (PI signal).

Immunofluorescence Staining

HeLa cells seeded on glass coverslips in 24-well plates (50,000 cells/well) were left to adhere for 18 h then treated for 24 h with **SBTub**s under "dark" or "lit" conditions as described above. Cover slips were washed then fixed with 0.5% glutaraldehyde, quenched with 0.1% $NaBH_4$, blocked with PBS + 10% FCS, and treated with rabbit alpha-tubulin primary antibody (abcam ab18251; 1:400 in PBS + 10% FCS) for 1 h; after washing with PBS, cells were incubated with goat-anti-rabbit Alexa fluor 488 secondary antibody (Abcam, ab150077; 1:400 in PBS + 10% FCS) for 1 h. After washing with PBS, coverslips were mounted onto glass slides using Roti-Mount FluorCare DAPI (Roth) and imaged with a Zeiss LSM Meta confocal microscope. Images were processed using Fiji software (Schindelin et al., 2012). Postprocessing was performed only to improve visibility. For maximum intensity projections, images were recorded at different focal planes by incrementally stepping through the sample (step size 1-2 μm) and maximum intensity projections were obtained using Fiji software.

EB1/EB3 Comet Assays with Whole-Sample Photoisomerisation

HeLa or A549 cells (12,000 or 40,000 cells/well, respectively) were seeded on 8-well ibiTreat μ slides (ibidi) 24 h prior to transfection with fluorescently-labeled end binding protein (Kleele et al., 2014). Cells were transiently transfected with *EB3-GFP*, *EB3-YFP* or

EB1-tdTomato plasmids using jetPRIME (Polyplus) or FuGENE 6 (Promega) reagents according to the manufacturers' instructions. Cells were imaged 24 h later, under 37°C and 5% CO_2 atmosphere. HeLa cells were imaged using an UltraVIEW Vox spinning disc confocal microscope (PerkinElmer) equipped with an EMCCD camera (Hammamatsu, Japan) and operated with *Volocity* software. A549 cells were imaged using a Nikon TiE microscope equipped with a Yokogawa CSU-W1 spinning disk confocal unit (50 μm pinhole size), an Andor Borealis illumination unit, Andor ALC600 laser beam combiner (405/488/561/640 nm), Andor IXON 888 Ultra EMCCD camera, and a Nikon 100× NA 1.45 oil immersion objective. The microscope was controlled by Nikon NIS Elements software (v.5.02.00). **SBTub** was added cautiously after focussing on cells on the microscope stage, and the compound was incubated for 5-10 min before imaging; this avoided exposure of the **SBTub** to any white focusing light, preventing unwanted isomerisation prior to imaging that could falsify results when testing for GFP/YFP orthogonality. Cells were imaged either at 488 nm (GFP; 23% laser power, 400 ms exposure time, 45 frames/min), 514 nm (YFP; similar parameters), or 561 nm (tdTomato; 20% laser power, 300 ms exposure time, 30 frames/min). Optionally for EB3 imaging, cells were additionally exposed, once per two minutes, to four consecutive frames (4×250 ms) of **SBTub**-isomerizing 405 nm light for compound activation. Optionally for EB1 imaging, 405 nm illuminations (10% laser power, 175 μs pixel dwell time) were re-applied at 2 min intervals during acquisition as indicated. For EB3 comet statistics, 6 cells per condition from three independent trials were taken; for EB1 statistics, 3 cells per condition. For photobleaching/orthogonality experiments, first-order exponential decay curves were fitted to each cell's comet count timecourses. EB3 count values were normalised to 100% at time zero, and EB1 counts were treated similarly or else normalised to 100% at the first return to plateau as appropriate; this enables intercomparison of cells with different starting comet counts (depending on their size, the position of the focal plane, etc). EB3 comets were counted with a *Fiji* software plugin based on the "Find maxima" function from the NIH; EB1 comets were counted in ImageJ using the ComDet plugin (E. Katrukha, University of Utrecht, https://github.com/ekatrukha/ComDet). Data are represented as mean comet count over time, with standard deviation, and scalebars in EB1 Videos are 10 μm.

Quantification of the Impact of SBTub3 on Live Cell MT Dynamics

HeLa cells were transfected with EB3-GFP using FuGENE 6 (Promega) according to manufacturer's instructions. Cells were imaged on a Nikon Eclipse Ti microscope equipped with a perfect focus system (Nikon), a spinning disk-based confocal scanner unit (CSU-X1-A1, Yokogawa) and an Evolve 512 EMCCD camera (Photometrics) with a stage top incubator INUBG2E-ZILCS (Tokai Hit) and lens heating calibrated for incubation at 37°C with 5% CO_2. Microscope image acquisition was controlled using MetaMorph 7.7. GFP was imaged at 491 nm (0.2 mW, 100 ms every 0.6 s) and full frame SBTub3 photoactivation was performed using 405 (0.1 mW, 100ms every 1.2 s), and images were acquired using a Plan Apo VC 60× NA 1.4 oil objective. Comet count analysis was performed in ImageJ using the ComDet plugin (E. Katrukha, University of Utrecht, Netherlands, https://github.com/ekatrukha/ComDet). Velocity analysis was performed in ImageJ using the MTrackJ plugin (Meijering et al., 2012).

EB3 Comet Assay with Cell-Specific Photoisomerisation

HeLa cells were transfected with *EB3-GFP* using FuGENE 6 (Promega) according to manufacturer's instructions. Cells were imaged on a Nikon Eclipse Ti microscope equipped with a perfect focus system (Nikon), a spinning disk-based confocal scanner unit (CSU-X1-A1, Yokogawa) and an Evolve 512 EMCCD camera (Photometrics) with a stage top incubator INUBG2E-ZILCS (Tokai Hit) and lens heating calibrated for incubation at 37°C with 5% CO_2. Microscope image acquisition was controlled using MetaMorph 7.7, with GFP imaging at 491 nm (0.17 mW, 300 ms every 2 s) and compound activation at 405 nm (77 μW, 100 ms every 90 s), and images were acquired using a Plan Apo VC 60× NA 1.4 oil objective. Comet count analysis performed in ImageJ using the ComDet plugin (E. Katrukha, University of Utrecht, https://github.com/ekatrukha/ComDet). Please see Data S1 Part G for more information.

EB3 Comet Assay in Rat Primary Hippocampal Neurons

All animal experiments were performed in accordance with Dutch law (Wet op de Dierproeven, 1996) and European regulations (Directive 2010/63/EU) under animal licence AVD1080020173404. All animal experiments were approved by the Dutch Animal Experiments Committee (DEC, Dier Experimenten Commissie) and were in line with the institutional guidelines of Utrecht University. Primary hippocampal neurons were derived from hippocampi of embryonic day 18 pups (male and female) from pregnant Wistar rats, cultured at 37°C and 5% CO_2 in supplemented NB, transfected with EB3-GFP at the 7th day *in vitro* (DIV 7) using Lipofectamine 2000 (Invitrogen), and imaged at DIV 10 in conditioned NB with 1% DMSO cosolvent (Kapitein et al., 2010, further details in the Supplementary Information). Cells were imaged on the Nikon Eclipse Ti system used for cell-specific photoisomerisation assays with similar conditions, except in that GFP was imaged at 491 nm (0.1 mW, 500 ms every 3 s). Neurons were initially imaged for EB3 for 10 min while a ROI (blue box) was pulsed with 405 nm light commencing 2 min into the acquisition, establishing baselines for EB3 activity in the cell and in the ROI (areas not pulsed with 405 nm but analysed in kymographs are boxed in orange and green); the ROI-pulsing protocol was to illuminate the ROI at 405 nm (95 μW, 7 ms per trace) tracing over the ROI 5 times every 3 s with imaging frames interleaved. The same neurons were then exposed to 1 μM **SBTub3** and immediately imaged for another 10 min using the same protocol. Images were processed in ImageJ, XY drift or movement was automatically compensated using the Template Matching plugin (Tseng et al., 2012) https://sites.google.com/site/qingzongtseng/template-matching-ij-plugin), comet count analysis was performed using the ComDet plugin (E. Katrukha, University of Utrecht, https://github.com/ekatrukha/ComDet).

QUANTIFICATION AND STATISTICAL ANALYSIS

All relevant assays were done in independent biological replicates. All attempts at replication were successful and no data were excluded from analysis. Blinding was not performed as assay readout is mostly unbiased (plate reader, flow cytometry, Fiji/ImageJ plugins). Microscopic evaluation was performed independently by two separate scientists. Data were analysed using Prism 8 software (GraphPad). Two-tailed unpaired t tests were used in pairwise group comparisons; * was used for $P < 0.05$, ** for $P < 0.01$, *** for $P < 0.001$, **** for $P < 0.0001$.